Emergent *s*-Wave Interactions between Identical Fermions in Quasi-One-Dimensional Geometries

Kenneth G. Jackson[1], Colin J. Dale[1], Jeff Maki[2], Kevin G. S. Xie[1], Ben A. Olsen[3],
Denise J. M. Ahmed-Braun[4], Shizhong Zhang[2], and Joseph H. Thywissen[1]

[1]*Department of Physics and CQIQC, University of Toronto, Toronto, Ontario M5S 1A7, Canada*
[2]*Department of Physics and HKU-UCAS Joint Institute for Theoretical and
Computational Physics at Hong Kong, The University of Hong Kong, Hong Kong, China*
[3]*Yale-NUS College, Singapore 138527, Singapore*
[4]*Department of Physics, Eindhoven University of Technology, The Netherlands*

Orbital degrees of freedom play an essential role in metals, semiconductors, and strongly confined electronic systems. Experiments with ultracold atoms have used highly anisotropic confinement to explore low-dimensional physics, but they typically eliminate orbital degrees of freedom by preparing atoms in the motional ground states of the strongly confined directions. Here, we prepare multiband systems of spin-polarized fermionic potassium (^{40}K) in the quasi-one-dimensional (q1D) regime and quantify the strength of atom-atom correlations using radio-frequency spectroscopy. The activation of orbital degrees of freedom leads to a new phenomenon: a low-energy scattering channel that has even particle-exchange parity along the q1D axis, as if the underlying interactions were *s*-wave. This emergent exchange symmetry is enabled by orbital singlet wave functions in the strongly confined directions, which also confer high-momentum components to low-energy q1D collisions. We measure both the q1D odd-wave and even-wave "contact" parameters for the first time and compare them to theoretical predictions of one-dimensional many-body models. The strength and spatial symmetry of interactions are tuned by a *p*-wave Feshbach resonance and by transverse confinement strength. Near resonance, the even-wave contact approaches its theoretical unitary value, whereas the maximum observed odd-wave contact remains several orders of magnitude below its unitary limit. Low-energy scattering channels of multi-orbital systems, such as those found here, may provide new routes for the exploration of universal many-body phenomena.

Subject Areas: Atomic and Molecular Physics,
Condensed Matter Physics

I. INTRODUCTION

Strong confinement of many-body systems has proven to be a fruitful approach for the creation of novel and emergent quantum states. For instance, the confinement of an electron gas in a two-dimensional quantum well with a strong perpendicular magnetic field leads to the manifestation of the integer and fractional quantum Hall effects, which exhibit exceptional transport properties [1]. Similarly, relaxing the electron spin degrees of freedom can result in the emergence of novel excitations such as skyrmions [2,3]. In ultracold atomic gases, recent advances in the manipulation of quantum gases in low dimensions have led to similar progress. For instance, fractional spin and charge degrees of freedom have been observed in

atomic gases under strong transverse confinement [4,5]. Moreover, confinement-induced resonances [6] can be used to change the interaction between atoms, providing a platform to investigate many-body physics in a disorder-free environment [7].

In studies with cold atoms, research has typically focused on regimes where transverse excitations along the strong confinement directions are irrelevant, with some exceptions, such as Ref. [8]. For instance, in a highly elongated trap, it is commonly assumed that the atoms occupy the lowest transverse oscillator state, such that the only active degrees of freedom are those along the weakly confined (axial) direction. As a result, three-dimensional (3D) systems of spin-polarized bosons and spin-half fermions under such confinement have been successfully modeled as quasi-one-dimensional (q1D) systems whose interactions are even-wave, i.e., described by one-dimensional (1D) pair wave functions that have exchange-even symmetry [6,9–15].

Here, we investigate the role of transverse orbital degrees of freedom in a simplified setting: a spin-polarized Fermi gas of ^{40}K with *p*-wave interactions confined in a q1D

geometry. By eliminating the spin degree of freedom, the possibility of spin-singlet *s*-wave scattering is excluded, so the role of orbital degrees of freedom is clearly exhibited. Our work builds on prior studies of odd-wave interactions, i.e., those described by 1D pair wave functions that have exchange-odd symmetry. Experimental works with low-dimensional *p*-wave systems have suppressed collisions along the strongly confined directions [16–19]. Q1D *p*-wave systems have been the subject of numerous theoretical studies [20–33], including a proposal to enable a *p*-wave halo dimer state [34,35] and to use strong confinement to reduce the three-body recombination loss [34,36] that plagues 3D *p*-wave gases [37–41].

In our experiment, we activate the orbital degrees of freedom through the controlled population of the first excited transverse band. We discover conditions under which fermions interact through wave functions with even particle-exchange symmetry for the q1D degree of freedom along the axial direction. We explain how fermionic symmetry is preserved by exchange-antisymmetric transverse orbital states. The magnetic Feshbach resonance used to tune *p*-wave interactions also adds an anisotropic nature to scattering. This vector character determines the magnetic-field values that can host emergent *s*-wave resonances and can be used to unambiguously identify the nature of the observed interactions.

We find clear signatures of interaction-induced correlations between atoms through rf spectroscopy for both odd- and even-wave scattering along the axial direction. Experimental investigations are supplemented by a theoretical analysis that reexamines the two-body problem and presents a unified treatment for arbitrary energies when multiple transverse bands are relevant. This allows us to describe emergent even-wave scattering on equal footing with odd-wave scattering and to relate this to novel correlations observed in rf spectroscopy. Specifically, we relate the high-frequency limit of the rf transfer rate between two internal spin states to the short-range correlations between atoms through universal contact relations [42–57]. Our theoretical treatment delineates the conditions under which the rf spin-flip rate is a measure of the 1D contact parameter. Notably, the rf spectra match true 1D scaling up to $2\omega_\perp$, where $\hbar\omega_\perp$ is the single-particle band gap. We extract the odd-wave contact parameter, anticipated by Refs. [27–29,31,32], and also measure the even-wave contact parameter [58–60]. A distinguishing feature of the latter is a novel singular structure at $2\omega_\perp$ that is anticipated by our analysis.

Our work suggests that introducing energy-gapped orbital degrees of freedom can be used more broadly to engineer the low-energy exchange symmetry of few-body and many-body systems. Our theoretical analysis provides a framework for understanding how these novel, orbit-dressed collision channels emerge from the one- to three-dimensional crossover. Both the conceptual paradigm and

the measurement protocols introduced here could be expanded to bosonic systems, spin mixtures, quasi-two-dimensional systems, and alternative partial waves.

This paper is structured as follows. In Sec. II, we provide an overview of the experimental protocol. In Sec. III, we describe *p*-wave scattering in the presence of strong q1D confinement and orbital degrees of freedom. Adapted to the experimental scenario, our treatment identifies three scattering continua with distinct pair wave functions. In Sec. IV, we measure the q1D odd-wave correlation strength and delineate the range of confinement strengths and magnetic fields in which the contact parameter is governed by the q1D odd-wave scattering length. We also demonstrate that the maximum contact parameter remains 2 orders of magnitude below its expected unitary value. In Sec. V, we present three experimental investigations of emergent *s*-wave interactions. The even-wave contact parameter approaches its expected unitary value, and we estimate that the inferred interaction strength is at least an order of magnitude stronger than that of odd-wave interactions. We conclude in Sec. VI with a summary of key findings and a discussion of future prospects enabled by multi-orbital scattering in low-dimensional systems.

II. EXPERIMENTAL PROTOCOL AND SUMMARY OF OBSERVATIONS

Our ensemble of q1D systems is prepared as follows. A bulk sample of ^{40}K, spin polarized in the lowest hyperfine-Zeeman state $|a\rangle$, is confined in an optical trap and cooled sympathetically with bosonic ^{87}Rb. After the final cooling stage, $N_{\text{tot}} = 7(1) \times 10^4$ spin-polarized ^{40}K atoms at $T \sim 300$ nK are loaded into a lattice of tubelike anisotropic traps [see Fig. 1(a)]. The confinement along the *x* and *z* directions is created by two orthogonal standing waves, produced with retroreflected beams of light with wavelength $\lambda_L = 760.6$ nm.

In the deep-lattice limit where tunneling between adjacent tubes can be neglected, each lattice site is harmonic near its minimum, with longitudinal oscillation frequency $\omega_y \approx 2\pi \times 400$ Hz. The transverse confinement, in turn, is set by the lattice depth V_L, measured in units of the recoil energy, $E_R = h^2/(2m\lambda_L^2) \approx h \times 8.6$ kHz, where *m* is the atomic mass of ^{40}K. With confinement in both transverse directions set to $V_L = 40\,E_R$, for instance, the transverse oscillation frequency is $\omega_\perp \approx 2\pi \times 100$ kHz. The transformation of the 3D cloud into an array of q1D clouds begins with a ramp of the lattice intensity, across a duration t_{ramp} (typically 300 ms), to a modest depth, less than $10\,E_R$ [Fig. 1(b)(i)]. Tubes are then isolated with a more rapid ramp to $40(2)\,E_R$. We use the loading model described in Appendix F to estimate the final number of atoms and temperature distribution in the tubes. For typical experimental parameters, the peak number per tube is $N \approx 30$ and $T/T_F \approx 0.8$, where T_F is the 1D Fermi temperature.
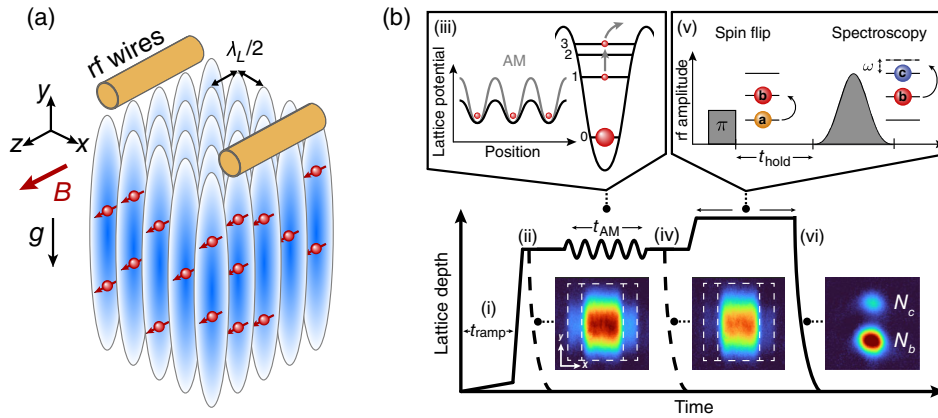
FIG. 1. Experimental overview. (a) Array of q1D traps aligned in the vertical (y) direction created by two orthogonal standing waves of light at wavelength λ_L. A static magnetic field B is oriented along z. Radio-frequency fields are generated by a pair of proximate microfabricated conductors. (b) Experimental sequence, depicting the potential depth of the confining two-dimensional optical lattice versus time. In part (i), we show that, following the creation of a degenerate Fermi gas, the optical standing waves are ramped on to generate the array of q1D traps. The two-part ramp includes a slow increase (in $t_{\rm ramp}$) to minimize heating followed by a fast jump to isolate q1D ensembles. Part (ii) shows that, at this stage, time-of-flight band mapping typically indicates that the majority of atoms are in the ground band (central dashed box), but some atoms are also loaded into the first excited band (lateral boxes). In part (iii), the lattice depth is optionally modulated for $t_{\rm AM}$ before being ramped to its full depth. The frequency is chosen to drive excited-band atoms resonantly into the third excited band, from which they leave the trap. In part (iv), time-of-flight images confirm that AM reduces population in the excited band. Part (v) shows that Feshbach-enhanced p-wave interactions are activated by a spin flip from $|a\rangle$ to $|b\rangle$. After a time $t_{\rm hold}$, the system is probed with a spectroscopic pulse at detuning ω. In part (vi), the fraction of atoms transferred from $|b\rangle$ to $|c\rangle$ by the spectroscopic rf pulse is measured with state-selective imaging.

Band populations are measured using band-mapped time-of-flight imaging. We adjust the chemical potential of the gas by tuning the optical trap depth and thereby optimizing for either ground-band loading or multiband loading. For the latter, when the chemical potential of the bulk gas is comparable to E_R, some atoms are loaded into the first excited state of each transverse direction since loading at the band edge cannot be adiabatic [Fig. 1(b)(ii)]. The fraction of atoms loaded into the first excited state is typically 15% in each direction.

To prepare for dedicated experiments measuring odd-wave correlations without orbital excitations (Sec. IV), we deplete the excited-band population using amplitude modulation (AM). The power of both optical standing waves is modulated for a time $t_{\rm AM}$ at a frequency resonant with the transition from the single-atom first-to-third excited bands [see Fig. 1(b)(iii)]. Because of the anharmonicity of the standing-wave confinement, this modulation is off-resonant from the zero-to-two excitation, leaving the number of atoms in the lowest band relatively unaffected. When optimizing for ground-band loading, band mapping after AM [Fig. 1(b)(iv)] indicates that the excited-band population is reduced to approximately 5% in each lattice direction. Lattice depth calibration is performed via AM of the single-particle zero-to-two excitation, with 5% uncertainty. Ensembles for even-wave correlation measurements (Sec. V) are prepared without AM or with phase modulation of the lattice to enhance population in the first excited bands (Appendix E).

With either preparation, the q1D ensembles of atoms in the lowest hyperfine-Zeeman state $|a\rangle$ are long-lived and weakly interacting. A p-wave Feshbach resonance [37–39] exists in the bb collision channel, where $|b\rangle$ is the second-lowest hyperfine Zeeman state, adiabatically connected to the $|F = 9/2, m_F = -7/2\rangle$ state at low magnetic field. After setting the field B and lattice depth V_L for a particular measurement, interactions are snapped on by transferring the atoms to the state $|b\rangle$ using a 40-μs-long rf pulse [see Fig. 1(b)(v)].

After a hold time $t_{\rm hold}$ of typically 160 μs, a spectroscopic pulse of duration $\tau = 120$ μs is applied. The frequency is offset ω above the single-particle $|b\rangle$-to-$|c\rangle$ resonant frequency, where $|c\rangle$ is the third-lowest hyperfine-Zeeman state (assumed to be weakly interacting; see Appendix C). The number of atoms transferred, N_c, is assessed by state-sensitive imaging after time-of-flight expansion, shown in Fig. 1(b)(vi). The spectroscopic pulse has a Blackman envelope to minimize Fourier broadening, such that the measured transfer rate Γ is given by N_c/τ times a corrective envelope factor.

Figure 2 provides a side-by-side comparison of correlations found with and without activated orbital degrees of freedom. The normalized rf transfer rate $\tilde{\Gamma} = E_F\Gamma/(\hbar\pi\Omega^2 N_{\rm tot})$ is shown versus lattice depth and magnetic field, where Ω is the Rabi frequency and E_F is the calculated Fermi energy of the central tube. As will be discussed in Sec. III A, Γ is proportional to short-range correlations, which are quantified by so-called contact
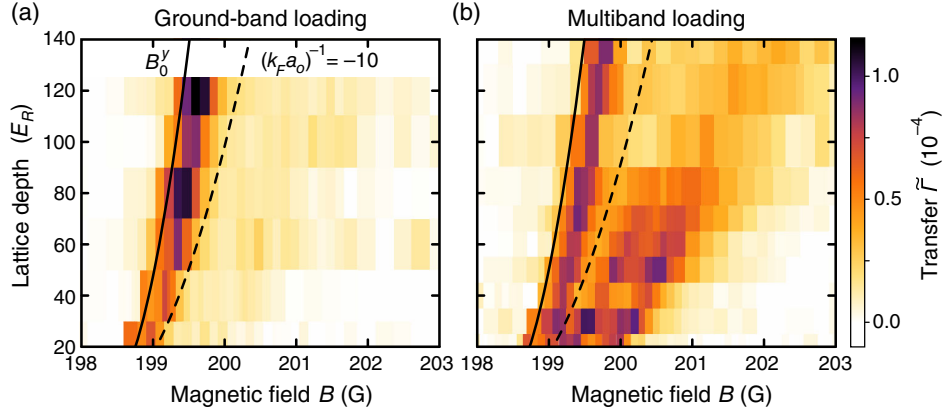
FIG. 2. Overview of observed correlations. The normalized rf transfer rate $\tilde{\Gamma}$, which is a measure of atom-atom correlation strength, is indicated by color across a range of magnetic fields and optical lattice depths. The depth of the confining optical lattice, V_L, is given in units of the recoil energy $E_R = h^2/2m\lambda_L^2$. The first peak in $\tilde{\Gamma}$ lies between the odd-wave resonance (indicated by a solid black line at B_0^y, where $a_o^{-1} = 0$ as discussed in Sec. III) and $(k_F a_o)^{-1} = -10$ (indicated by a black dashed line). Panel (a) shows that, without active orbital degrees of freedom, atom-atom correlations are found only within this range. Panel (b) shows that, with multiband loading, correlations beyond the odd-wave regime are found. We show that these additional correlations are due to even-wave interactions along the q1D direction. The structure of $\tilde{\Gamma}(B, V_L)$ is further explored in Figs. 5–8.

parameters [42–57] and have been the subject of prior experimental studies in 3D for both *s*-wave and *p*-wave systems [55,61–63] and in quasi-two-dimensional systems with *s*-wave interactions [64,65].

Without active orbital degrees of freedom, atom-atom correlations are found just above the odd-wave resonance (B_0^y as defined later) indicated by a solid line in Fig. 2(a). At B_0^y, the q1D odd-wave scattering length a_o is predicted to diverge because of interactions along the longitudinal direction. The observed normalized transfer rate $\tilde{\Gamma}$ is largest at magnetic fields between B_0^y and where $a_o = -(10k_F)^{-1}$ (dashed line), where k_F is the Fermi momentum in the central tube. In Sec. IV, we show that the observed correlations agree well with those expected from weakly attractive odd-wave interactions.

Figure 2(b) displays the same quantities, but with orbital degrees of freedom activated. The normalized rf transfer rate $\tilde{\Gamma}$ now reveals that atom-atom correlations appear well beyond the odd-wave parameter range (still bracketed by the solid and dashed lines). In Sec. V, we provide a clear assignment of these correlations to even-wave interactions and compare their strength to that predicted by theory.

III. *p*-WAVE SCATTERING IN A QUASI-ONE-DIMENSIONAL TRAP

Low-energy scattering in the q1D trap has been considered previously for even-wave scattering [6,9–15] of both identical bosons and spin mixtures of fermions, as well as for odd-wave scattering [20–26,34,35] of identical fermions. These treatments consider atoms to reside in the ground state of the transverse confinement, such that higher-energy orbital states are only relevant as closed channels. Our experimental scenario requires a generalization that includes

the population of asymptotic states with transverse orbital excitation. When these additional orbital states are hybridized with 3D *p*-wave dimer states, whose internuclear separation is typically much smaller than the transverse oscillator length, the new scattering resonances that emerge include both even- and odd-wave q1D symmetries.

To obtain the effective scattering parameters in q1D, let us first recall that the *p*-wave scattering amplitude in 3D, f_{3D}, is given by

$$-(kf_{3D})^{-1} = i + (V_{3D}k^3)^{-1} + (kR_{3D})^{-1} + \mathcal{O}(k), \quad (1)$$

where V_{3D} and $R_{3D} > 0$ are the *p*-wave scattering volume and effective range, respectively, and $\hbar k$ is the relative momentum. Near a *p*-wave Feshbach resonance, V_{3D} is widely tunable [66–68], but the Wigner bound [69–71] constrains the maximum value of R_{3D} to be on the order of the van der Waals length, which is small compared to typical k^{-1} in the ultracold regime. Thus, $(kR_{3D})^{-1} \gg 1$, and according to Eq. (1), it remains numerically important for 3D *p*-wave resonant scattering. In fact, it is crucial to include the effective-range term in Eq. (1) to describe many physical properties of *p*-wave Fermi gases appropriately [54,55,71–76].

Now, let us consider a Fermi gas of identical atoms, such as ^{40}K in a single hyperfine-Zeeman state, confined in a highly anisotropic potential. The single-particle Hamiltonian within a single tube is, neglecting anharmonic corrections,

$$H_0 = \frac{1}{2m}p^2 + \frac{1}{2}m(\omega_x^2 x^2 + \omega_y^2 y^2 + \omega_z^2 z^2), \quad (2)$$

where $p = (p_x, p_y, p_z)$ is the 3D momentum of the atom. Quasi-one-dimensional confinement is achieved when the

transverse harmonic frequencies in the x and z directions are much larger than in the y direction: $\{\omega_x, \omega_z\} \gg \omega_y$. This allows a separation of energy scales, in which the collision energy (determined by the 1D Fermi energy E_F at low temperature, $T \lesssim E_F/k_B$) is much smaller than the energy quanta of the transverse motion, namely, $E_F \ll \{\hbar\omega_x, \hbar\omega_z\}$. For a true 1D system of $N \gg 1$ spinless fermions, the Fermi energy is $E_F = N\hbar\omega_y$, so the condition for q1D collisions is

$$N\lambda \ll 1, \tag{3}$$

where $\lambda \equiv \omega_y/\omega_\perp$ is the trap aspect ratio, written in the case of cylindrically symmetric confinement, $\omega_x = \omega_z \equiv \omega_\perp$. For our typical confinement strength and atom numbers (see Sec. II), $N\lambda \sim 0.1$, i.e., well within the q1D regime.

A. Scattering in q1D regime

For noninteracting atoms of equal mass, the two-body Schrödinger equation can be separated into center-of-mass (c.m.) and relative (rel) motion, each described by a Hamiltonian with the same form as Eq. (2) except for the replacement of the mass m with the total mass $2m$ or the reduced mass $\mu = m/2$, respectively [77–80]. In the limit $N \gg 1$, we can treat the relative momentum k along the q1D axis (y) as continuous but retain the quantization of the transverse motion. Note that $\hbar$ has been set to unity here and for the remainder of this subsection.

In the c.m. frame, setting $\omega_x = \omega_z = \omega_\perp$ and $\omega_y = 0$, we can write the two-body Hamiltonian as

$$H_{0,2b} = \frac{1}{2\mu} p_{\text{rel}}^2 + \frac{1}{2}\mu\omega_\perp^2 \rho^2, \tag{4}$$

where p_{rel} is the relative momentum and $\rho = \sqrt{x^2 + z^2}$ (and ϕ below) are the standard cylindrical coordinates. The noninteracting relative wave function can be characterized conveniently by the principal quantum number in the radial direction, $\mathcal{N}$, and the azimuthal quantum number m. Up to a normalization factor, the transverse spatial wave functions of the noninteracting eigenstates are

$$\Psi_{\mathcal{N},m}(\rho, \phi) = \frac{e^{im\phi}\rho^{|m|}}{a_\perp^{|m|+1}} e^{-\frac{\rho^2}{2a_\perp^2}} \mathcal{L}_{\mathcal{N}}^{|m|}(\rho^2/a_\perp^2), \tag{5}$$

where $\mathcal{L}_{\mathcal{N}}^{|m|}(x)$ is the generalized Laguerre polynomial and $a_\perp = \sqrt{1/\mu\omega_\perp}$ is the radial oscillator length. Including the kinetic energy in the 1D direction, $k^2/(2\mu)$, the energies of the full $|\mathcal{N}, m, k\rangle$ states are $E_{\mathcal{N},m,k} = (k^2/2\mu) + (2\mathcal{N} + |m| + 1)\omega_\perp$, which we also write in dimensionless form as

$$\mathcal{E}_m \equiv \frac{E_{\text{rel}} - (|m|+1)\omega_\perp}{2\omega_\perp} = \left(\frac{ka_\perp}{2}\right)^2, \tag{6}$$

where E_{rel} is the total energy not including the c.m. motion or c.m. confinement.

Now, let us include the interatomic interaction described in detail in Appendix A. We assume for now that the interaction is cylindrically symmetric, such that m remains a good quantum number; the extension to anisotropic interactions is discussed in Sec. III C. For an underlying *p*-wave interaction, interacting eigenstates can be sorted into $m = -1$, $m = 0$, and $m = +1$ and will, in general, be a superposition of $|\mathcal{N}, m, k\rangle$ states with different $\mathcal{N}$.

The symmetry of the asymptotic wave function along the axial direction can be seen in the emergent 1D wave functions, which are solely a function of y. For an incident wave with momentum k in continuum $\mathcal{N}$ and with symmetry m, the scattered wave component with quantum numbers $\mathcal{N}'$ and m' is given by

$$\psi_{\mathcal{N}',m',k}(y) = \delta_{m',m}\left[\delta_{\mathcal{N}',\mathcal{N}} e^{iky} + f_{\mathcal{N}'}^{(m)} e^{-\frac{2}{a_\perp}\sqrt{\mathcal{N}'-\mathcal{E}_m - i\varepsilon}|y|} \left(\frac{y}{|y|}\right)^{|m|+1}\right], \tag{7}$$

where ε is an infinitesimal positive quantity. Here, $f_{\mathcal{N}'}^{(m)}$ are the scattering amplitudes into the $\mathcal{N}'$ radial state,

$$f_{\mathcal{N}'}^{(0)} = -i\mu k T_o$$

and $\quad f_{\mathcal{N}'}^{(\pm 1)} = -i\mu \frac{a_\perp}{2} \frac{\sqrt{\mathcal{N}'+1}\sqrt{\mathcal{N}+1}}{\sqrt{\mathcal{E}_1 - \mathcal{N}' + i\varepsilon}} T_e, \tag{8}$$

parametrized by odd-wave and even-wave scattering transition matrices (T-matrices) T_o and T_e, which are defined below.

For the $m = 0$ sector, the two-body wave function is exchange symmetric along the transverse direction, as is evidenced by Eq. (5) under parity transformation $\phi \to \phi + \pi$. The overall exchange antisymmetry of the two-body wave function then requires the axial wave function to be *antisymmetric* under exchange, as is observed in the scattered wave of Eq. (7). Thus, two particles undergo odd-wave scattering along the q1D direction (also called 1D *p*-wave scattering).

Consider the incident state $|\mathcal{N} = 0, m = 0, k\rangle$ just above the lowest noninteracting band energy, such that $\mathcal{E}_0 \ll 1$. The interacting wave function consists of all $|\mathcal{N}, m = 0, k\rangle$ states, starting with $\mathcal{N} = 0$, for which both atoms are in the single-particle ground-state orbital of the transverse confinement potential. From Eq. (7), we see that for higher-energy states with $\mathcal{N}' > 0$, the associated evanescent scattering wave vanishes for $|y| \gg a_\perp$. Therefore, only the component with $\mathcal{N}' = 0$ and $m = 0$ survives

asymptotically, a state that describes two particles in the single-particle ground state of the transverse oscillator.

For the $m = 1$ and $m = -1$ sectors, the transverse wave function is odd [see, again, Eq. (5) for $\phi \to \phi + \pi$] such that the scattering wave function is exchange symmetric along y, the longitudinal direction [81,82]. Consider an incoming state $|\mathcal{N} = 0, m = 1, k\rangle$, with collision energies just above the lowest-energy $m = 1$ band, such that $\mathcal{E}_1 \ll 1$. Similarly to the $m = 0$ sector, we see from Eq. (7) that all the $\mathcal{N}' > 0$ components of the scattered wave function decay at $|y| \gg a_\perp$. Therefore, the asymptotic q1D wave function features a transverse component that is characterized by $\mathcal{N} = 0$ and $m = 1$. Similar arguments hold for the $m = -1$ sector.

The separation between the odd- and even-wave channels in the presence of interactions leads to two low-energy scattering matrices. For $m = 0$, and in the low-energy limit $[0 < \mathcal{E}_0 = (E_{\mathrm{rel}} - \omega_\perp)/2\omega_\perp \ll 1]$, we find that the effective 1D scattering T matrix T_o is given by

$$T_o^{-1} = \frac{2\mu}{2}\left[\frac{1}{a_o} + k^2 r_o + ik\right], \quad \text{with}$$

$$\frac{1}{a_o} = \frac{a_\perp^2}{6}\left(\frac{1}{V_{3D}} + \frac{2}{R_{3D}a_\perp^2}\right) - \frac{2}{a_\perp}\zeta(-1/2)$$

$$\text{and} \quad r_o = \frac{a_\perp^2}{6R_{3D}} + \frac{a_\perp}{4}\zeta(1/2), \tag{9}$$

where $\zeta(s) \equiv \zeta(s, 1)$ is the Riemann zeta function, a_o is the 1D odd-wave scattering length, and $r_o > 0$ is the 1D odd-wave effective range. The key steps in our derivation are described in Appendix A. These equations define the effective 1D parameters for the odd-wave scattering amplitude f_o as

$$-f_o^{-1} = 1 - i(a_o k)^{-1} - i r_o k + \mathcal{O}(k^3). \tag{10}$$

This result connects the strongly confined laboratory scenario to a scattering theory with a true 1D form and is consistent with previous calculations of p-wave scattering in strongly confined q1D systems [20–26,34]. Effective scattering in the $m = 0$ sector asymptotically resembles that of a spinless Fermi gas in 1D.

Unitary odd-wave scattering, for which $f_o \to -1$, extends across the range of collision momenta $|a_o|^{-1} \ll k \ll r_o^{-1}$. The effective range r_o decreases with stronger transverse confinement because it scales as $a_\perp^2/R_{3D}$ and thus as $\omega_\perp^{-1}$. Experiments in this universal regime have not yet been realized because a typical $k_F r_o$ is of order unity; thus, the effective-range contribution must be kept. The persistent relevance of r_0 is due to the large ratio between the (optical) confinement length scale and the 3D effective range: λ_L/R_{3D} is approximately 300. We also note that since the q1D approach uses a 3D interaction model at short range, our treatment would break down for

$a_\perp \lesssim R_{3D}$. The question of universality is discussed further in Sec. III D.

For atoms in the lowest even-wave scattering continuum, i.e., $\mathcal{N} = 0$ and $m = \pm 1$, or equivalently $0 < \mathcal{E}_1 = (E_{\mathrm{rel}} - 2\omega_\perp)/2\omega_\perp \ll 1$, the even-wave T matrix T_e in the low-energy limit reduces to

$$T_e^{-1} = \frac{2\mu}{2}\left[-a_e + k^2 r_e + \frac{i}{k}\right], \quad \text{with}$$

$$a_e = -\frac{a_\perp}{2}\left[\frac{a_\perp^3}{6V_{3D}} + \frac{2a_\perp}{3R_{3D}} + \zeta(-1/2) + \zeta(1/2)\right]$$

$$\text{and} \quad r_e = \frac{a_\perp^3}{16}\left[\frac{4a_\perp}{3R_{3D}} + \zeta(1/2) + \zeta(3/2)\right], \tag{11}$$

where a_e is the 1D even-wave scattering length and $r_e > 0$ is the 1D even-wave effective range. (See Table I for a summary of scattering parameters.) This result is identical to a 1D calculation with true s-wave interactions [6,9–15] with the effective range r_e included. The corresponding 1D even-wave scattering amplitude is

$$-f_e^{-1} = 1 + ia_e k - ir_e k^3 + \mathcal{O}(k^5). \tag{12}$$

Compared to the odd-wave effective range term in Eq. (9), we see that the effective-range term, $k^3 r_e$ here, is smaller than kr_o by a factor of $k^2 a_\perp^2$, which must be small in the q1D limit. As a result, both the resonant $k|a_e| \ll 1$ and zero-range $k^3 r_e \ll 1$ limits are achieved at low energy, with no necessary hierarchy between a_e and r_e. At the largest lattice depth in our experiments, $k_F^3 r_e \sim 0.1$, which enables q1D even-wave scattering to enter a universal regime in which the effective range can be neglected.

B. RF spectrum

The T matrices (9) and (11) allow us to calculate the rf line shape because, at high frequency, the rf spectrum is related to the short-range correlations in the many-body system. Our starting point is the relation between Γ and the 3D correlation strength [45,83]:

$$\Gamma(\omega) = \frac{\Omega^2}{4}\mathrm{Im}\, i \int dt e^{i(\omega + i\varepsilon)t} \int d^3\mathbf{R} \int d^3\mathbf{r}$$

$$\times \left\langle T_t \hat{\psi}_b^\dagger \hat{\psi}_c\left(\mathbf{R} + \frac{1}{2}\mathbf{r}, t\right)\hat{\psi}_c^\dagger \hat{\psi}_b\left(\mathbf{R} - \frac{1}{2}\mathbf{r}, 0\right)\right\rangle, \tag{13}$$

TABLE I. Summary of notation used to parametrize scattering in this work.

Resonance type	Scattering amplitude	Scattering parameters
3D p-wave	f_{3D}	V_{3D}, R_{3D}
1D odd-wave	f_o	a_o, r_o
1D even-wave	f_e	a_e, r_e

where Ω is the Rabi frequency, r and R are the relative and center-of-mass positions, T_t is the time-ordering operator, and $\hat{\psi}_b$ and $\hat{\psi}_c$ are the fermionic annihilation operators for a fermion in hyperfine-Zeeman states $|b\rangle$ and $|c\rangle$, respectively. Full expressions for the transfer rate are reported in Appendix B. In the experimentally relevant regime, where $\omega \gg E_F$ and $\omega < 4\omega_\perp$,

$$\Gamma^{(0)}(\omega) = \frac{\Omega^2 C_o}{2}\left[\frac{\theta(\omega)}{\omega^{3/2}} + \frac{\theta(\omega - 2\omega_\perp)\sqrt{\omega - 2\omega_\perp}}{\omega^2}\right] \quad (14)$$

and

$$\Gamma^{(\pm 1)}(\omega) = \frac{\Omega^2 C_e^{(\pm 1)}}{2}\left[\frac{\theta(\omega)}{\omega^{5/2}} + \frac{2\theta(\omega - 2\omega_\perp)}{(\omega - 2\omega_\perp)^{1/2}\omega^2}\right], \quad (15)$$

where C_o is the 1D odd-wave contact, $C_e^{(\pm 1)}$ are the 1D even-wave contacts, and $\theta(x)$ is the Heaviside step function. In both expressions, the first term represents the contribution from those continuum states that are below the first orbital gap. The step function $\theta(\omega - 2\omega_\perp)$ in the second term indicates the opening of a new transverse band, when the rf photon energy exceeds the energy difference from the $\mathcal{N} = 1$ scattering continuum, thus making the final scattering states within the new transverse band available. Each continuum has a density of states that scales as $1/\sqrt{\mathcal{E}_m}$, as is characteristic of a 1D system. This gives rise to a cusplike $(\omega - 2\omega_\perp)^{1/2}$ dependence for $\Gamma^{(0)}$ and a singular dependence $(\omega - 2\omega_\perp)^{-1/2}$ for $\Gamma^{(\pm 1)}(\omega)$. The latter is observed experimentally; see Sec. V B.

As discussed in Appendix B, both Eqs. (14) and (15) are constrained to match the odd-wave contact relation with a characteristic $\omega^{-3/2}$ spin-flip rate for $\omega < 2\omega_\perp$ [27],

$$\lim_{E_F/\hbar \ll \omega < 2\omega_\perp} \Gamma^{(0)}(\omega) = \frac{\Omega^2}{2}\sqrt{\frac{2\mu}{\hbar}}\frac{C_o}{\omega^{3/2}}, \quad (16)$$

and the even-wave contact relation with a leading $\omega^{-5/2}$ rate,

$$\lim_{E_F/\hbar \ll \omega < 2\omega_\perp} \Gamma^{(\pm 1)}(\omega) = \frac{\Omega^2}{2}\frac{1}{\sqrt{2\hbar\mu}}\frac{C_e^{(\pm 1)}}{\omega^{5/2}}, \quad (17)$$

where factors of $\hbar$ have now been restored. These relations will be used to find the contact parameters in the measured spectra.

C. Anisotropic interactions

Our treatment so far has assumed isotropic 3D interactions and radially symmetric trapping potentials. For the experimental system, however, interactions are anisotropic: the 3D xy dimer branch is split by $\Delta E_{\mathrm{dd}}/h \sim 100$ kHz from the 3D z dimer branch due to dipole-dipole interactions in ^{40}K [84],

leading to direction-dependent scattering volumes V_{3D}^i and effective ranges R_{3D}^i, where $i = x$, y, or z [see Fig. 1(a) for axis orientation]. Furthermore, the cylindrical anisotropy can be tuned by adjusting the confinement strength independently along the x and z axes, as depicted by Fig. 3(a) in the case of $\omega_z > \omega_x$.

For broken cylindrical symmetry, $\mathcal{N}$ and m are no longer good quantum numbers. Instead, we use n_x and n_z to index quanta of relative motion in the Cartesian axes of confinement [85] and write the states as $|n_x, n_z, k\rangle_{\mathrm{rel}}$. Even parity in y occurs for odd $n_x + n_z$, and vice versa. The exchange antisymmetry of the $|1_x, 0_z\rangle_{\mathrm{rel}}$ and $|0_x, 1_z\rangle_{\mathrm{rel}}$ states can be seen by decomposing them back into a single-particle basis. Labeling the colliding particles A and B, a $|1\rangle_{\mathrm{rel}}$ state with no c.m. excitation is $(|1\rangle_A|0\rangle_B - |0\rangle_A|1\rangle_B)/\sqrt{2}$ or, in other words, a singletlike state in which two particles share a single quantum of orbital excitation.

The emergence of q1D resonances is due to the hybridization of the 1D bands of scattering states with p-wave dimers that are now labeled as x, y, and z dimers due to dipole splitting [see Table II and Fig. 3(a)]. Because of the symmetry of the 3D dimers, a selection rule arises regarding the coupling to the scattering states. For example, the x dimer has the short-range symmetry corresponding to the spherical harmonic $Y_{1x} \sim x/r$. As a result, the x dimer can only be hybridized with continuum states in the $|1_x, 0_z, k\rangle_{\mathrm{rel}}$ band above the threshold energy $E_{\mathrm{zp}} + \hbar\omega_x$, where E_{zp} is the zero-point energy $\frac{1}{2}\hbar(\omega_x + \omega_z)$. The magnetic field at which this crossing occurs is labeled B_0^x in Fig. 3(a). Similar analyses also apply to the y and z scattering: the y dimer enhances odd-wave scattering within the $|0_x, 0_z, k\rangle_{\mathrm{rel}}$ band, and the z dimer enhances even-wave scattering in the $|0_x, 1_z, k\rangle_{\mathrm{rel}}$ band (see Table II). The three distinct resonances are shown in Fig. 3(a) and are labeled in order of increasing magnetic field: B_0^y ("zeroth"), B_0^x ("first"), and B_0^z ("second"). The nature of the scattering state is illustrated in Figs. 3(d)–3(f).

In the presence of anisotropic interactions, we still calculate the q1D scattering parameters using Eqs. (9) and (11), but we now replace V_{3D} and R_{3D} with the values of V_{3D}^i and R_{3D}^i specific to the underlying 3D resonance [68]. The low-energy scattering parameters in Eqs. (9) and (11) can then be tuned by changing the 3D scattering parameters in order to engineer arbitrarily strong odd- or even-wave interactions.

In terms of the 3D quasi-bound-state energy [68,84], approximately $-\hbar^2 R_{\mathrm{3D}}^i/(2\mu V_{\mathrm{3D}}^i)$, the resonance condition $a_o^{-1} = 0$ for odd-wave scattering is, from Eq. (10),

$$-\frac{\hbar^2 R_{\mathrm{3D}}^y}{2\mu V_{\mathrm{3D}}^y} = E_{\mathrm{zp}}\left[1 - 6\frac{R_{\mathrm{3D}}^y}{a_\perp}\zeta(-1/2)\right], \quad (18)$$

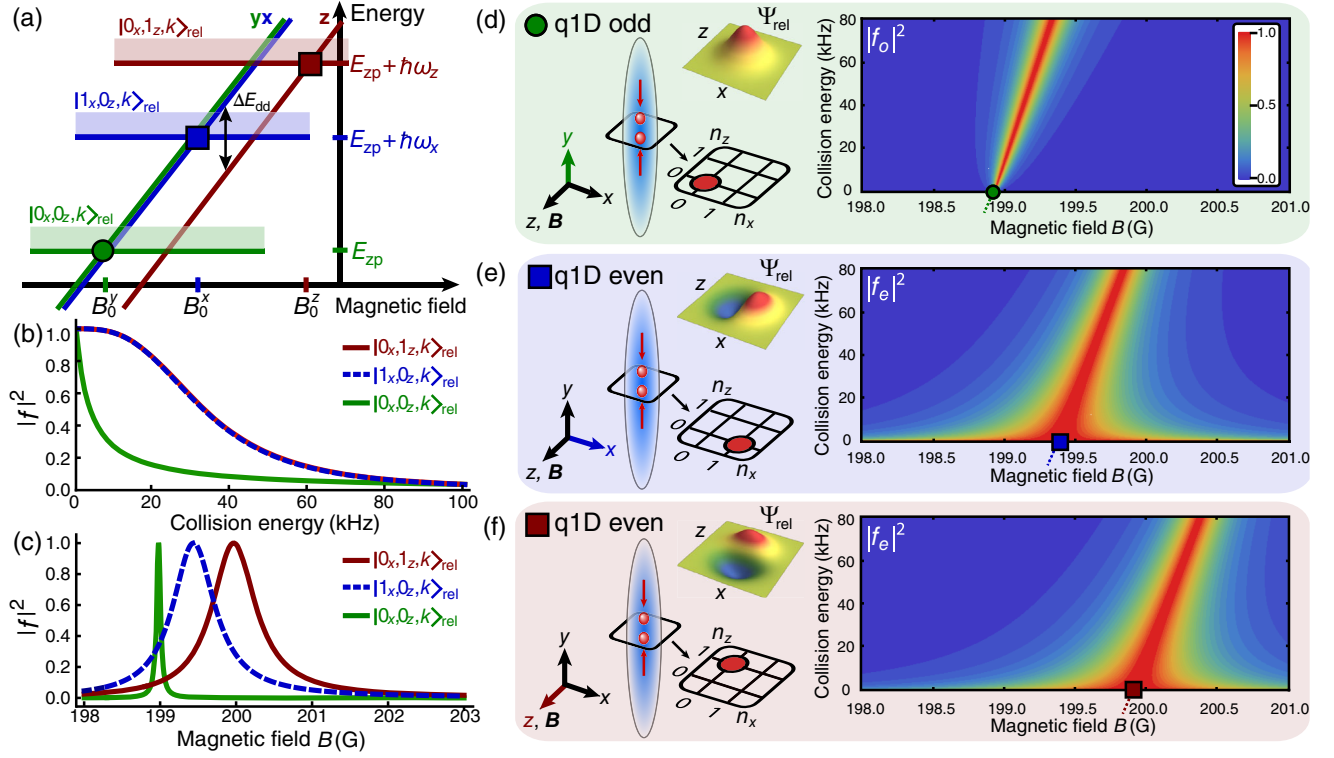while for even-wave scattering, the resonant conditions ($a_e^x = 0$ or $a_e^z = 0$) are, from Eq. (12),

FIG. 3. Scattering resonances in q1D. (a) Asymptotic states $|n_x, n_z, k\rangle_{\mathrm{rel}}$ with confinement energies of $(n_x + 1/2)\hbar\omega_x + (n_z + 1/2)\hbar\omega_z$ plus a continuum of $\hbar^2 k^2/2\mu$ from motion along y. The three lowest continua, shown here, become strongly interacting when magnetically tuned to resonance with an appropriate 3D p-wave dimer state (labeled x, y, and z). The resonant location for $|1_x, 0_z, k\rangle_{\mathrm{rel}}$ states (blue square at B_0^x) is at an energy shifted above the ground band by the transverse excitation energy $\hbar\omega_x$. The resonance for $|0_x, 1_z, k\rangle_{\mathrm{rel}}$ states (red square at B_0^z) is further displaced by the dipole-dipole splitting ΔE_{dd} of the xy and z dimer states and any cylindrical asymmetry for which the case $\omega_z > \omega_x$ is shown. Corrections to this approximate picture are given by Eqs. (18) and (19). (b) Effective 1D scattering cross section $|f|^2$ at resonance versus q1D collision energy. The broader resonance for asymptotic states with $n_x = 1$ or $n_z = 1$ states can be attributed to their even-wave character, as discussed in the text. (c) $|f|^2$ versus magnetic field, for a typical in-tube scattering energy of 10 kHz. (d) q1D odd-wave continuum characterized by a transverse wave function $\Psi_{\mathrm{rel}}(x, z)$ with even spatial parity. A contour plot shows the $|f_o|^2$ versus magnetic field and collision energy. (e,f) q1D even-wave continua, each characterized by an asymptotic transverse wave function $\Psi_{\mathrm{rel}}(x, z)$ with odd spatial parity. The contour plots of $|f_e|^2$ versus magnetic field and collision energy combine the trends of panels (b) and (c) and emphasize the growing magnetic width in the $k \to 0$ limit that is characteristic of s-wave collisions. Scattering amplitudes in panels (b)–(f) are based on Eq. (10) with parameters in Eq. (9), or Eq. (12) with parameters in Eq. (11), with equal $V_L^x = V_L^z = 40E_R$.

$$-\frac{\hbar^2 R_{\mathrm{3D}}^{x,z}}{2\mu V_{\mathrm{3D}}^{x,z}} = (E_{\mathrm{zp}} + \hbar\omega_{x,z})$$

$$\times \left\{ 1 + \frac{3}{2} \frac{R_{\mathrm{3D}}^{x,z}}{a_\perp} [\zeta(1/2) + \zeta(-1/2)] \right\}. \quad (19)$$

Since $R_{\mathrm{3D}}^i/a_\perp$ is typically small in our experiments, these relations show that resonant odd- and even-wave scattering

TABLE II. Exchange parity and spatial orientation of the two-atom states in the lowest three scattering continua.

Continuum	Asymptotic state	Transverse parity	q1D parity	Resonant dimer
Zeroth	$|0_x, 0_z, k\rangle_{\mathrm{rel}}$	Even	Odd	y dimer
First	$|1_x, 0_z, k\rangle_{\mathrm{rel}}$	Odd	Even	x dimer
Second	$|0_x, 1_z, k\rangle_{\mathrm{rel}}$	Odd	Even	z dimer

occurs approximately when the 3D quasi-bound state reaches the relevant scattering continuum, as depicted in Fig. 3(a).

The interaction anisotropy is observed in radio-frequency spectroscopy and thus the contact parameters. We note that the odd-wave contact relation is only governed by the interactions along the y direction, so Eq. (14) is not altered. On the other hand, even-wave interactions now appear as x and z correlation peaks at distinct magnetic-field values, instead of the degenerate $m = \pm 1$ correlation peaks in Eq. (15). Asymptotic rf transfer rates are now proportional to C_e^x and C_e^z, respectively.

D. Width of the universal regime

The qualitative departure of even-wave scattering from odd-wave scattering is illustrated from its energetic width,

i.e., the scaling of elastic scattering versus momentum k of the q1D collision. Figures 3(b)–3(f) show the scattering probabilities $|f_o|^2$ and $|f_e|^2$, as a function of both energy and magnetic field. A key feature is the enhanced width, in either parameter, of $|f_e|^2$. Near resonance, the energy range of unitary scattering is determined by the effective-range term of Eqs. (10) and (12). For odd-wave interactions, this energetic width can be characterized by $\Delta_o \equiv (\hbar^2/2\mu)r_o^{-2}$, while for even-wave interactions, the energetic width is $\Delta_e \equiv (\hbar^2/2\mu)r_e^{-2/3}$. From Eqs. (9) and (11), we find that $\Delta_o/\Delta_e = 18^{2/3}(R_{3D}/a_\perp)^{4/3}$, which is small in experiments. This behavior is illustrated in Fig. 3(b) on resonance, which is a vertical cut at the resonant magnetic field in the contour plots of $|f_{o,e}|^2$ seen in panels (d)–(f).

If a_e is tuned to zero [for instance, at $B = B_0^z$ defined by Eq. (19)], then the unitary limit $f_e \rightarrow -1$ is achieved for $r_e k^3 \ll 1$. The range of scattering energies in which this occurs is given by $\hbar^2 k^2/2\mu \lesssim \Delta_e$. In terms of transverse confinement strength, the leading-order width is [86]

$$\Delta_e \approx \hbar\omega_\perp (3\sqrt{2}R_{3D}/a_\perp)^{2/3}. \tag{20}$$

Within a degenerate Fermi gas, the range of two-body collision energies is $2E_F$. Scattering is unitary when the energetic width $\Delta_e \gtrsim 2E_F$, or

$$N\lambda \lesssim (3R_{3D}/2a_\perp)^{2/3}. \tag{21}$$

The rhs of Eq. (21) is around 0.2 for the confinement strength typically used in low-dimensional quantum gas experiments and thus poses a comparable constraint to the q1D criterion $N\lambda \ll 1$. For the $N\lambda \sim 0.1$ conditions in our experiments, resonant even-wave scattering is already energetically broad [see Fig. 3(b)].

Elastic odd-wave collisions also have a zero-range limit. A parallel argument finds that when $|a_o|^{-1} \rightarrow 0$, the energetic width of the unitary regime ($\Delta_o = \hbar^2/2\mu r_o^2$) is $\Delta_o \approx \hbar\omega_\perp (18R_{3D}^2/a_\perp^2)$ to leading order [87]. Comparing this width to $2E_F$, one finds that the confinement condition for $\Delta_o \gtrsim 2E_F$ is

$$N\lambda \lesssim (3R_{3D}/a_\perp)^2. \tag{22}$$

The rhs of Eq. (22) is about 0.02 for our typical conditions; thus, it is much more restrictive than the q1D criterion, and it is not satisfied for our experiments.

The magnetic width of low-energy resonant scattering reveals qualitatively different scaling in the odd- and even-wave cases. From Eq. (10), at constant a_o, as $k \rightarrow 0$, we see that $|f_o|^2 \rightarrow 0$, and scattering is thus progressively narrower in B at lower energy [Fig. 3(d)]. A similar analysis for Eq. (12), however, shows that $f_e \rightarrow -1$ for a progressively broader range in B at lower energy [Figs. 3(e) and 3(f)]. At a constant scattering energy, both odd- and even-wave resonances become broader in field with increasing confinement. However, the odd-wave field width scales with the square root of the lattice depth, while the even-wave field width scales linearly with lattice depth. Therefore, confinement can lead to a significantly broadened resonance for even-wave scattering, even though the energetic width of the underlying 3D resonance is still narrow [88].

In the zero-range limit identified here, the emergent even-wave scattering channel has a solitary relevant parameter that is tunable. This provides a regime in which a spin-polarized Fermi gas can be considered universal. Without the need for effective-range terms, its behavior can be understood with models independent of the particular element used in experiments, similar to 3D fermionic spin mixtures near an s-wave scattering resonance or two-dimensional bosons near their noninteracting fixed point [89,90].

IV. OBSERVATION OF ODD-WAVE CORRELATIONS

We probe odd-wave interactions by performing rf spectroscopy at magnetic fields near B_0^y using the procedure outlined in Sec. II. Figure 4 shows the dimensionless transfer fraction $\tilde{\Gamma}(\tilde{\omega})$ versus dimensionless rf detuning $\tilde{\omega} \equiv \hbar\omega/E_F$, both rescaled by the calculated Fermi energy of the central tube (see Appendix F). Correlations are revealed by an asymmetric spectrum, i.e., spectral weight that appears at a large positive ω but not at a large negative ω of equal magnitude. The strength of correlations can be
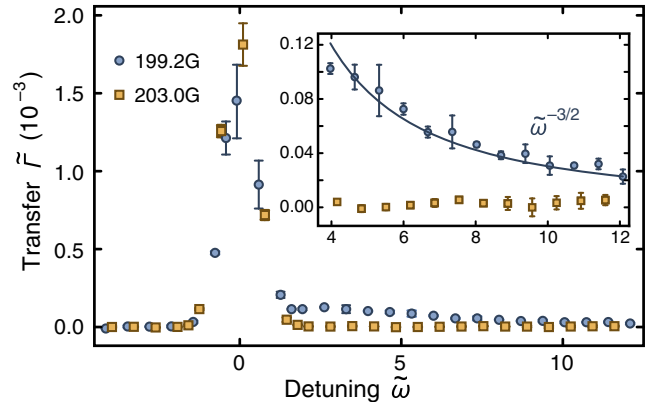

FIG. 4. RF spectrum of odd-wave interactions. The normalized rf transfer rate $\tilde{\Gamma}$ versus dimensionless detuning $\tilde{\omega}$ from the single-particle resonance [see Fig. 1(b)(v)]. Two spectra are shown, both for $V_L = 40E_R$: at $B = 203.0$ G (squares), the gas is weakly interacting; at $B = 199.2$ G (circles), odd-wave interactions are Feshbach enhanced [$-1/k_F a_o \sim 5$; see Fig. 2(a)]. The interacting gas shows an increased $\tilde{\Gamma}$ for positive $\tilde{\omega}$. The inset shows $\tilde{\Gamma}(\tilde{\omega})$ on the same axes, with a $\tilde{\omega}^{-3/2}$ fit to the high-frequency tail of the interacting spectrum, allowing the determination of C_o from Eq. (14). Error bars represent one standard deviation.

quantified through Eq. (16), in the range $4 \lesssim \tilde{\omega} \lesssim 15$ (for which $\omega < 2\omega_\perp$), where we observed the characteristic $\tilde{\omega}^{-3/2}$ power-law decrease. In the strongly interacting regime, we fit the experimental data to extract C_o, thereby measuring the odd-wave correlations in a q1D ultracold gas for the first time, to our knowledge. At magnetic fields far from resonance, correlations are weak, and there is no observable asymmetry, as can be seen in the inset of Fig. 4.

Figure 5 shows the contact strength and atom number measured across a range of magnetic fields and lattice depths. The contact was measured using the transfer fraction at a single frequency, typically $\tilde{\omega} = 5$, which fulfills the condition $E_F/\hbar \ll \omega < 2\omega_\perp$ and selects the first term of Eq. (14). Since we are optimizing for ground-band loading, we can assume that $\Gamma^{(\pm1)} \ll \Gamma^{(0)}$,

which allows for a single-shot determination of the contact:

$$\frac{\tilde{C}_o}{N} = 4\sqrt{2}\pi\tilde{\omega}^{3/2}\tilde{\Gamma}, \tag{23}$$

where

$$\tilde{C}_o \equiv \frac{4m}{\hbar^2 k_F} C_o \tag{24}$$

is the dimensionless odd-wave contact [91].

The observed value of $\tilde{C}_o/N$ is up to 2×10^{-2}, with the maximum near the q1D scattering resonance. In Figs. 5(b) and 5(d), both atom loss and correlations shift to higher magnetic field with increasing lattice depth, primarily due to the increasing zero-point energy $E_{\rm zp}$ associated with the transverse harmonic confinement. When comparing Figs. 5(a) and 5(b), or comparing Fig. 5(c) and 5(d), we see that field-dependent data collapse to a single curve when plotted as a function of $-1/k_F a_o$, indicating that we are probing the physics in the q1D regime.

Consider first the weakly repulsive regime. No significant correlations are seen in the range $-20 < -1/k_F a_o < -2$, which can be understood from Fig. 3(a): the 3D quasibound p-wave dimer has yet to emerge above the odd-wave scattering threshold. Similar to the 3D p-wave case [55], we conclude that the dimer state is not significantly populated. For stronger repulsive interactions [92], $-5 \lesssim -1/k_F a_o < 0$, a finite $\tilde{C}_o$ is observed; however, concurrently with strong losses, which are perhaps due to the instability of the repulsive odd-wave gas, its value remains small.

Next, consider the regime with relatively weak attractive interactions, $4 \lesssim -1/k_F a_o \lesssim 15$. In the absence of strong loss, we can compare the measured values of C_o to equilibrium calculations: zero-temperature Bethe ansatz theory [31] and a high-temperature expansion theory [32] (Appendix D). These are shown in Fig. 5(a). The theory band for the high-temperature expansion reflects the weak 1D effective-range dependence on lattice depth and includes a correction for the inhomogeneous density and tube number discussed in Appendix F. In this weakly interacting regime, the measurements overlap with both the zero-temperature and the high-temperature predictions, with no adjustable parameters, and they follow the anticipated monotonic decrease with a_o^{-1}.

At higher magnetic fields, where $-1/k_F a_o \gtrsim 15$, the apparent contact deviates from these predictions. We attribute this departure to overlapping even-wave correlations (see Sec. V), due to a remaining population in the excited bands, such that Γ can no longer be associated purely with $\Gamma^{(0)}$.

Finally, consider magnetic fields close to resonance $(B \sim B_0^y)$, where we observe a smaller contact than is anticipated by theory. The unitary high-temperature value of the contact is $\tilde{C}_o/N = 8/\pi$ in a uniform system [32] while at zero temperature $\tilde{C}_o/N = 4/\pi$ [27,29,93]. This far
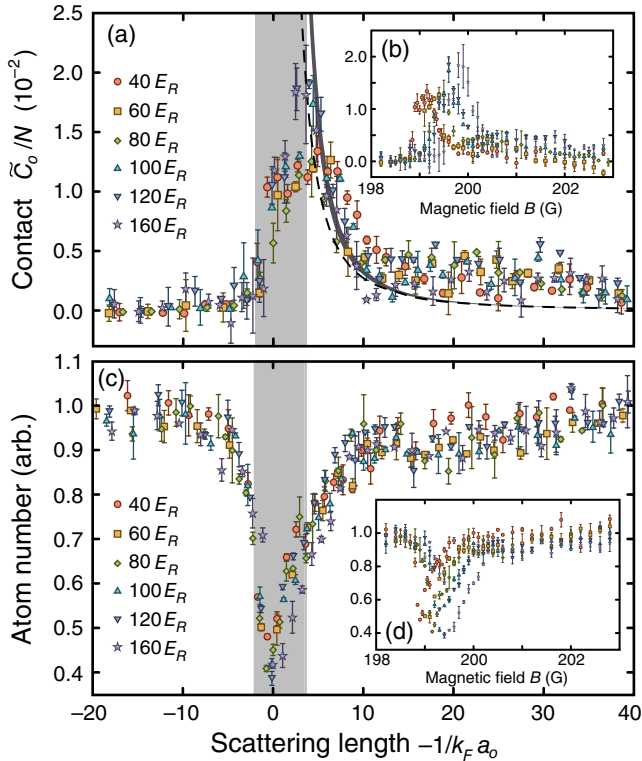

FIG. 5.   Odd-wave contact and loss. (a) Contact per atom versus odd-wave scattering length, $-1/k_F a_o$. Per Eq. (23), the dimensionless odd-wave contact per atom is related to the scaled transfer from spectroscopy. The zero-temperature Bethe ansatz prediction for $k_F r_o = 1$ is shown by the dashed-black line, and the high-temperature prediction for $T/T_F = 0.8$ is shown as a band covering the range of experimental lattice depths. (b) Inset: same $\tilde{C}_o/N$ data versus magnetic field, emphasizing the data collapse in (a). (c) Total atom number after the spectroscopy sequence, as a fraction of initial atom number, shown as a function of $-1/k_F a_o$. In the gray-shaded parameter range, 30% or more of the atoms are lost. The peak loss occurs at the calculated $a_o^{-1} = 0$. (d) Inset: atom-number data as a function of magnetic field. Error bars in this figure represent one standard deviation.

exceeds the highest $\tilde{C}_o/N$ observed. Instead, within the range $-2 \lesssim -1/k_F a_o \lesssim 4$, indicated in Fig. 5(c) with a gray band, the contact per atom is decreased. This is attributed to the onset of strong loss: we find that more than 30% of the initial population is lost by the end of t_{hold}, from which we infer a three-body loss coefficient $L_3 \geq 10^{-5}$ cm^2/s. As in prior studies of atom loss in q1D Fermi gases [18,19], we find that the loss rate is independent of lattice depth, as indicated by the data collapse in Fig. 5(c).

Limited by losses, the system does not develop a contact parameter larger than $\tilde{C}_o/N \sim 2 \times 10^{-2}$. We can interpret this magnitude by estimating the odd-wave interaction energy that would be found in an equilibrium cloud with the same correlation strength and negligible effective range. The adiabatic relation for 1D odd waves is [27]

$$\frac{\partial F}{\partial(-a_o^{-1})} = C_o, \qquad (25)$$

where F is the free energy of the gas. Integrating under the observed contact outside of the loss-dominated regime, we find that between $(-k_F a_o)^{-1} = 10$ and $(-k_F a_o)^{-1} = 4$, the interaction energy is $\Delta F \sim -0.03\, N E_F$. Therefore, at least in the conditions realized here, an odd-wave Fermi gas can be stable only in the weakly interacting regime.

V. OBSERVATION OF EVEN-WAVE CORRELATIONS

We now turn our attention to the features that appear when multi-orbital loading is allowed, i.e., those features appearing in Fig. 2(b) but not in Fig. 2(a). In order to test the hypothesis that these spectral features are due to q1D even-wave correlations and to elucidate their nature, we undertook a sequence of experiments: spectroscopy with variable asymmetric confinement (Sec. V A), spectroscopy at variable frequency (Sec. V B), and spectroscopy with variable coupling strength (Sec. V C). The sample preparation common to all these tests does not use AM (see Sec. II and Appendix E), such that about 15% of the atoms are in each of the transverse excited bands as measured by band mapping.

A. Vector character of the even-wave resonances

The resonance condition for even-wave interactions is given by Eq. (19), which, for our small value of $R_{3D}/a_\perp$, can be approximated for the $i = x$ or $i = z$ continua as

$$-\frac{\hbar^2 R_{3D}^i}{2\mu V_{3D}^i}\bigg|_{B=B_0^i} \approx E_{\text{zp}} + \hbar\omega_i, \qquad (26)$$

where the lhs is the 3D *p*-wave dimer energy, linear in B, as shown in Fig. 3(a). The incorporation of an extra vibrational excitation quantum (shared between the atoms in a $|1_x\rangle_{\text{rel}}$ or $|1_z\rangle_{\text{rel}}$ motional state) shifts the even-wave

resonances from the odd-wave resonance condition, which is

$$-\frac{\hbar^2 R_{3D}^y}{2\mu V_{3D}^y}\bigg|_{B=B_0^y} \approx E_{\text{zp}}, \qquad (27)$$

from Eq. (18). In the following, we investigate the dependence of B_0^i on ω_i.

Figure 6(a) shows $\tilde{\Gamma}(B)$ at $V_L = 40E_R$, a depth at which three distinct peaks can be resolved in multiband loading. To subtract the common shift from the zero-point energy, we show the displacements of each peak (ΔB_{0th}, ΔB_{1st}, and ΔB_{2nd}) from B_0^y [94]. Since $\Gamma = \sum \Gamma^i$, additional tests are necessary to confirm the origin of these peaks.

The first peak also appears with a ground-band loading procedure [as shown in Figs. 6(a) and 2(a)], so it can be unambiguously associated with odd-wave interactions. As shown in Fig. 5, the correlation peak is not at the resonance location, due to strong loss near resonance. For the parameters of Fig. 6, the magnetic-field location of the peak correlation B_{0th} is shifted about 0.2 G above B_0^y.

A vector assignment of these two higher peaks can be made using unequal confinement, $V_L^x \neq V_L^z$, whose anticipated effect on B_0^x and B_0^z is illustrated in Fig. 3(a) for $\omega_z > \omega_x$. Figure 6(b) shows the best-fit peak displacements ΔB_{0th}, ΔB_{1st}, and ΔB_{2nd} from repeated $\tilde{\Gamma}(B)$ scans at variable V_L^z, with fixed $V_L^x = 40E_R$. We see how ΔB_{1st} is insensitive to V_L^z (similarly to ΔB_{0th}) while ΔB_{2nd} has a stronger dependence on V_L^z. Based on this trend, we can conclude that the peak at B_{2nd} must be associated with confinement along the z direction, which would be expected for the even-wave threshold B_0^z, where scattering states hybridize with the 3D z dimer.

Cylindrical symmetry is broken in our experiments by the applied magnetic-field direction (z) orthogonal to the q1D direction (y). The field aligns the magnetic dipole moments of ^{40}K and thus splits the Feshbach resonances for the two even-wave features (see Sec. III C). This 0.5-G splitting is evident upon the comparison of B_{1st} and B_{2nd} at equal lattice depth, which is $V_L^z = 40E_R$ for Fig. 6.

A similar experimental study with variable V_L^x and fixed V_L^z indicates that the peak at B_{1st} is associated with confinement along x. In summary, the vector character and dependence on the lateral confinement is consistent with the assignment of the correlation peak at B_{1st} in Fig. 6 to the x even-wave continuum, and at B_{2nd} to the z even-wave continuum.

B. Spectroscopic signatures

The strongest evidence for the observation of even-wave correlations in our system comes from the functional form of the rf spectra. As discussed in Sec. III B, within the range of frequencies $\omega < 2\omega_\perp$, in which a q1D system resembles a true 1D system, the rf transfer rate should scale as $\omega^{-5/2}$
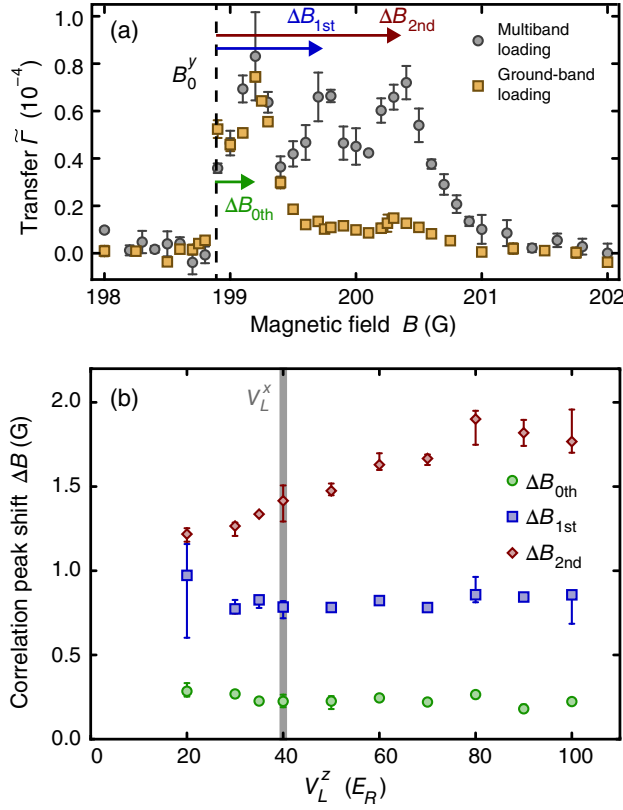
FIG. 7.   Even-wave rf spectrum. Dimensionless rf transfer rate $\tilde{\Gamma}$ versus detuning ω, for a multiband-loaded ensemble at 200.5 G, with $V_L = 80\,E_R$. Between $0.7\omega_\perp$ and $1.7\omega_\perp$, the signature even-wave scaling $\tilde{\Gamma} \propto \omega^{-5/2}$ is observed [see Eq. (B5)]. The solid lines show Eq. (15), with a free vertical scale factor. The singularity in the transfer rate (a unique signature of 1D even waves) manifests as a peak near $\omega \approx 2\omega_\perp$, as described in the main text. The inset shows $\tilde{\Gamma}(\omega)$ on a linear vertical scale in the $\omega^{-5/2}$ regime; a single-parameter fit determines the sum of the even-wave contacts. For these conditions, $k_F a_e^z \approx 0.4$, compared to $k_F a_e^x \approx 1.6$, so scattering is dominated by the $|0_x, 1_z, k\rangle_{\rm rel}$ states. Error bars here represent one standard deviation.

FIG. 6.   Vector assignment of the second even-wave correlation peak. (a) Normalized rf transfer rate $\tilde{\Gamma}$ at constant $\tilde{\omega} \approx 5$ versus magnetic field B applied in the z direction. Three peaks in $\tilde{\Gamma}(B)$ are resolved for multiband loading (circles), while a single clear peak is observed for ground-band loading (squares). Here, confinement is cylindrically symmetric, with $V_L^x = V_L^z = 40\,E_R$. The magnetic-field displacements from the resonance position B_0^y are indicated for maximum $\tilde{\Gamma}$ by colored arrows and reported as ΔB in the subsequent panel. Error bars in panel (a) represent one standard deviation. (b) Magnetic-field displacements for the three peaks in $\tilde{\Gamma}(B)$ shown for variable V_L^z, with fixed $V_L^x = 40\,E_R$. While $B_{0\rm th}$ and $B_{1\rm st}$ shift with the zero-point energy included in B_0^y, $B_{2\rm nd}$ has a stronger dependence on V_L^z. This trend supports the hypothesis that the third resolved peak in $\tilde{\Gamma}$ versus B corresponds to scattering in the z continuum, whose energy is $\hbar\omega_z$ above the odd-wave continuum. This coincides with the resonance condition for even-wave scattering, Eq. (26); more direct evidence of even-wave character is given in Sec. V B. Best-fit peak centers in panel (b) are calculated by fitting to three Gaussians with the Monte Carlo Bootstrap method, and the asymmetric error bars represent 67% confidence intervals.

(as opposed to $\omega^{-3/2}$ found for odd-wave correlations in Sec. IV). Furthermore, for larger rf frequencies, $\tilde{\Gamma}(\omega)$ should exhibit a singularity at $\omega = 2\omega_\perp$: see Eq. (15). The experimentally measured $\Gamma(\omega)$ is a sum of all Γ^i, but it will be dominated by only one Cartesian component near its resonant magnetic field.

Figure 7 shows the rf spectrum observed at $B \approx B_{1\rm st}$. For frequencies between $0.7\omega_\perp$ and $1.7\omega_\perp$, we observe a clear
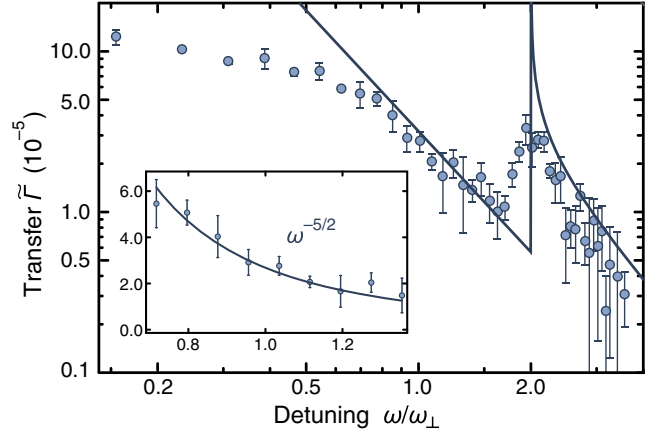
$-5/2$ power law consistent with 1D s-wave correlations (see Fig. 7 inset). In this region, it is possible to extract the 1D even-wave contact parameters $C_e^{x,z}$. We note that once C_e^x and C_e^z are fixed, the general form of $\tilde{\Gamma}(\omega)$ [Eq. (B2) and, in particular, Eq. (15)] is then determined for higher frequencies, no matter what the relative strengths of C_e^x and C_e^z are. We do not understand why the $-5/2$ power law does not extend to lower frequencies, below $0.7\omega_\perp/2\pi \sim 90$ kHz. This may be due to incomplete equilibration of the long-wavelength degrees of freedom [95–97].

A sharp peak in $\tilde{\Gamma}(\omega)$ appears, as anticipated, at twice the band gap [98]. Here, atom pairs are promoted from incident states with principal radial quantum number $\mathcal{N} = 0$ to final states with $\mathcal{N} = 1$ and hyperfine-Zeeman state $|c\rangle$. Since rf transitions cannot modify the spatial wave functions, the presence of the feature demonstrates that the scattering states are dressed by higher-$\mathcal{N}$ orbital states at short range, i.e., $y \lesssim a_\perp$ in Eq. (7). The singular feature in the theory results from a combination of two factors: the divergence of the 1D density of final states (see Sec. III B) and the k-independent even-wave matrix element [see the $|m| = 1$ term of Eq. (A1)]. As observed, the $2\omega_\perp$ singularity is softened by the distributions of a finite range of collision energies, the average over variable lattice depths of 1D tubes, and the Fourier broadening of the rf pulse.

The observation of these two even-wave signatures in $\Gamma(\omega)$ gives strong evidence for the emergence of effective s-wave correlations in the q1D gas.

C. Even-wave contact parameter

The correlations appearing in Fig. 2(b) across a broad range in magnetic field can now be quantified through the even-wave contact. At each magnetic field, the even-wave contacts $C_e^{x,z}$ can be probed with a single-shot measurement of Γ at a fixed detuning with the range $0.7\omega_\perp \lesssim \omega \lesssim 1.7\omega_\perp$, as discussed in Sec. V B. In the regime where $\Gamma^{(0)} \ll \Gamma^{(x,z)}$, we find

$$\tilde{C}_e^x + \tilde{C}_e^z = 2\sqrt{2}\pi N \tilde{\omega}^{5/2} \tilde{\Gamma}, \qquad (28)$$

where

$$\tilde{C}_e^{x,z} \equiv \frac{4m}{\hbar^2 k_F^3} C_e^{x,z} \qquad (29)$$

is the dimensionless even-wave contact. Since only about 15% of atoms populate each transverse excited band, we base k_F on the total atom number, just as in the odd-wave case. We show in Appendix E that rf transfer is proportional to the excited-band population, motivating us to report the contact divided by the number of atoms in one single-particle motional excited band N_1, which we assume to be equal for both the x and z directions. In Fig. 8, we report $\tilde{C}_e/N_1$ for various interaction strengths, tuning the scattering length a_e^z across a range of 200G to 205G, away from the odd-wave feature. We observe data collapse between different lattice depths and single-shot detunings $\omega \sim \omega_\perp$ chosen to be within the $-5/2$ power-law regime described in Sec. V B.

For $k_F a_e^z \gtrsim 2.5$, the observed trend matches that of a high-temperature model (Appendix D) that maps the imbalanced band mixture in our system onto a spin mixture with true 1D *s*-wave interactions. For the large lattice depths in Fig. 8, the distinct even-wave resonances overlap [see Fig. 2(b)], and the slightly larger a_e^x is shown on the upper axis of Fig. 8. Both experiment and theory include both x and z even-wave interactions. However, in the region of interest, correlations are dominated by even-wave z pairing, as indicated by the agreement with a solid line that shows $\tilde{C}_e^z/N_1$ alone.

For $0 \leq k_F a_e^z \lesssim 2$, the observed $\tilde{C}_e/N_1$ plateaus to 0.5(1). The expected near-unitary contact can be estimated using a zero-temperature theory [60] developed for 1D *s*-wave spin mixtures, again using a mapping of imbalanced band populations to imbalanced spin populations in the model. In the homogeneous case, we find $\tilde{C}_e^z/N_1 \approx 1.0$, on the same order of magnitude as the observed value. A full description of the unitary regime would need to include loss [see inset of Fig. 8], inhomogeneity, and the contribution of C_e^x. The contrast with the q1D odd-wave case, where the observed contact is at most 10^{-2} of the unitary value, is already striking.
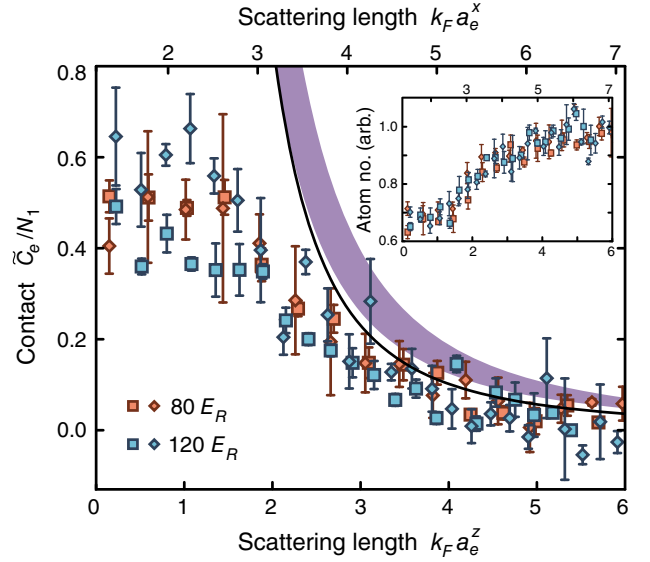

FIG. 8. Even-wave correlations. The even-wave contact $\tilde{C}_e = \tilde{C}_e^x + \tilde{C}_e^z$ normalized by N_1 is plotted versus even-wave scattering lengths a_e^z (bottom) and a_e^x (top). The scattering lengths a_e are tuned by the magnetic field across a range of 200 G to 205 G and scaled by the calculated k_F of the central tube. Single-shot measurements of C_e use Eq. (28), repeated here for two different single-shot detunings: $\omega/2\pi = 100$ kHz (squares) and $\omega/2\pi = 125$ kHz (diamonds). Two lattice depths are shown: red and blue points are $80E_R$ and $120E_R$, respectively. The shaded purple band gives a high-temperature expansion prediction for $\tilde{C}_e^x/N_1 + \tilde{C}_e^z/N_1$, from Eq. (D5), with no fit parameters. The width of the band reflects one standard deviation of systematic uncertainties (atom number and band-population fractions) and the variation of effective-range contributions. Both experiment and theory include both x and z even-wave interactions. However, in the region of interest, correlations are dominated by even-wave z pairing: a solid line shows $\tilde{C}_e^z/N_1$ alone. The inset shows the relative atom number after spectroscopy, for the same ranges of $k_F a_e^z$ (bottom) and $k_F a_e^x$ (top). Error bars represent one standard deviation.

We can interpret the strength of the observed contact using the adiabatic relation from 1D *s*-waves [59]:

$$\frac{\partial F}{\partial a_e^z} = C_e^z. \qquad (30)$$

Assuming thermal equilibrium, the interaction energy is then found by integrating under the observed contact, which contains contributions from both x and z resonances but is dominated by $\tilde{C}_e^z$. As a lower estimate for the total interaction energy, we find that between $k_F a_e^z = 5$ and $k_F a_e^z = 2$, it is around $\Delta F \sim -0.2 N_1 E_F$, whereas integrating between $k_F a_e^z = 5$ and $k_F a_e^z = 0$, we find $\Delta F \sim -0.7 N_1 E_F$. The q1D even-wave gas is thus strongly interacting, with an attractive energy that is at least an order of magnitude larger than is observed in the low-loss range of the odd-wave interactions.

We can understand the enhanced strength of q1D even-wave interactions through the proportionality of p-wave coupling to momentum, as indicated by Eq. (A1). For odd waves, the relevant momentum that leads to a finite interaction is in the y direction, along the tube. For even waves, p-wave coupling is achieved through the transverse gradient in the spatial wave function, which is proportional to $a_\perp^{-1}$ [see Eq. (A2)]. For a typical momentum k_F, the ratio of even- to odd-wave coupling is thus $2/a_\perp^2 k_F^2$, which is of order $1/N\lambda$, and thus necessarily large in the q1D regime.

VI. DISCUSSION AND CONCLUSION

The extension of low-dimensional systems to include multi-orbital scattering opens the door to several new prospects. We have shown that one result is the emergence of q1D even-wave interactions in a spin-polarized Fermi gas. The range of many-body physics accessible with this new interaction channel will be constrained by atom loss, including the three-body recombination. Odd-wave atom loss processes have been studied both theoretically [36] and experimentally [18,19]; similar studies in the q1D even-wave scenario, which also address band relaxation, are needed.

Future work could also include a more detailed understanding of rf spectra, as shown in Figs. 4 and 7, especially the low-frequency deviations from the high-frequency power law. In this regime, the subleading contacts, conjugate to r_o for odd waves [32] and r_e for even waves, are expected to appear as additional higher-order power-law contributions to the rf spectral function Γ.

A shallow q1D dimer state lies below threshold both in the repulsive $a_o > 0$ gas and in the attractive $a_e > 0$ gas probed in our experiment. Searching for these dimer states and characterizing their stability would further examine the paradigm of an emergent q1D symmetry. In the even-wave case, the binding energy is expected to be large even near resonance.

Another prospect is to search for emergent s-waves in quasi-two-dimensional (q2D) ensembles of identical fermions. A similar mechanism would apply: that antisymmetric orbital wave functions in a strong confinement direction would enable exchange-even collisional wave functions in the low-energy q2D degrees of freedom. In either q1D or q2D, a study of the universal dynamics and thermodynamics would be an interesting comparison to true s-wave systems.

Using a multichannel framework, new universal contact relations should be found to clarify, for instance, the correspondence to the closed-channel fraction. Qualitatively, a q1D (or q2D) polarized gas with emergent s-wave interactions is expected to be similar to a spin mixture with true s-wave interactions. However, for systems such as metastable helium [99,100] or dipolar gases with strong spin-orbit relaxation [101], spin polarization is necessary for collisional stability. For fermionic isotopes in these systems, emergent

s-wave interactions in the quasi-low-dimensional regime could provide a new pathway to low-energy universality.

The paradigm introduced here can be extended to higher partial waves. For example, it could be used to study bosons with d-wave interactions [102–104]. The d-wave generalization of Eq. (A2) would have $m = 0$, $|m| = 1$, and $|m| = 2$ components. The $|m| = 1$ matrix element would be proportional to $kk'/a_\perp^4$ and would enable odd-wave scattering, i.e., emergent q1D p-wave interactions between identical bosons, which is forbidden by exchange symmetry in true 1D systems. The even-m matrix elements would be proportional to $1/a_\perp^6$, which is in contrast to free space, where low-energy d-wave scattering is suppressed at low k. Analogous to the emergent q1D s-wave observed here, strong confinement enhances coupling by the high momentum of the confined wave function.

In summary, our study provides a comprehensive understanding of the behavior of quasi-one-dimensional fermions interacting with short-range p-wave interactions. Our observations and analyses reveal that multi-orbital scattering in strongly confined systems opens the door to the exploration of alternate exchange symmetries in low-energy scattering channels. The energy dependence of higher partial-wave scattering is dominated by the inter-orbital gap, which offers a new approach to suppressing finite-range corrections and studying universal many-body phenomena. Our work indicates the potential of cold-atom experiments with fully activated orbital, spin, and mass degrees of freedom, whose interplay gives rise to a wealth of phenomena in electronic materials.

ACKNOWLEDGMENTS

APPENDIX A: q1D LIMIT OF p-WAVE SCATTERING

To incorporate the correct momentum dependence of p-wave scattering, a model interatomic pseudopotential $U(y, \rho)$ can be written in the following way. Given two arbitrary two-body states ϕ and χ, the matrix element of U is

$$\langle \phi | U | \chi \rangle = g \boldsymbol{\nabla} \phi^*(\mathbf{0}) \cdot \boldsymbol{\nabla} \chi(\mathbf{0}), \qquad (A1)$$

evaluated at zero separation between the two fermions, where g is a coupling constant [21,25,105–107]. We note

that the potential, as written, is isotropic. In the q1D regime, the relevant two-particle states are denoted as $|\mathcal{N}, m, k\rangle$, and the matrix elements of U are

$$\langle \mathcal{N}', m', k'|U|\mathcal{N}, m, k\rangle$$
$$= \frac{g}{\pi a_\perp^2} kk' \delta_{m,0} \delta_{m,m'}$$
$$+ \frac{2g}{\pi a_\perp^4} \sqrt{\mathcal{N}+1} \sqrt{\mathcal{N}'+1} \delta_{|m|,1} \delta_{m,m'}, \quad (A2)$$

where $\hbar$ and atomic mass factors have been suppressed. Since the relative wave function vanishes as $\Psi_{\mathcal{N},m} \propto \rho^{|m|}$, this pseudopotential only has nonzero matrix elements for $|m| \leq 1$. The structure of Eq. (A2) is as follows. The first term on the rhs corresponds to $m = 0$, where the gradient operator acts along the y direction (parallel to k and k'). This produces the correct form factor for odd-wave scattering in the q1D direction, kk'. As a result, it inherits the low-momentum behavior of the 3D p-wave scattering and vanishes at low energy. On the other hand, the second term corresponds to the gradient operator acting along the transverse directions and, as such, requires antisymmetric radial wave functions ($m = \pm 1$) to give rise to a nonvanishing matrix element. This term is proportional to a constant at low k and k', which is a hallmark of s-wave scattering.

The matrix elements in Eq. (A2) carry forward to a similar structure for the low-energy T matrix in the q1D geometry, which we take to have the following form:

$$\langle \mathcal{N}', m', k'|T_{\text{q1D}}|\mathcal{N}, m, k\rangle$$
$$= \frac{kk'}{\pi a_\perp^2} T_{\text{q1D}}^{(0)}(E_{\text{rel}}) \delta_{m,0} \delta_{m,m'}$$
$$+ \frac{2}{\pi a_\perp^4} \sqrt{\mathcal{N}+1} \sqrt{\mathcal{N}'+1} T_{\text{q1D}}^{(m)}(E_{\text{rel}}) \delta_{|m|,1} \delta_{m,m'}, \quad (A3)$$

where $T_{\text{q1D}}^{(m)}$ is the T matrix in the q1D geometry with relative angular momentum m. To evaluate $T_{\text{q1D}}^{(m)}$, we make use of its relation to the free-space T matrix, T_{3D} [10]:

$$T_{\text{q1D}}^{(m)}(E_{\text{rel}})$$
$$= T_{\text{3D}}^{(m)}(E_{\text{rel}})$$
$$+ T_{\text{3D}}^{(m)}(E_{\text{rel}})[G_{\text{q1D}}^{(m)}(E_{\text{rel}}) - G_{\text{3D}}^{(m)}(E_{\text{rel}})] T_{\text{q1D}}^{(m)}(E_{\text{rel}}), \quad (A4)$$

where $G_{\text{q1D}}^{(m)}$ and $G_{\text{3D}}^{(m)}$ are the propagators in the q1D geometry and 3D free space, respectively, with definite angular momentum m, and $T_{\text{3D}} = -(2\pi/\mu k^2) f_{\text{3D}}$.

Equation (A4) can be evaluated analytically for both the odd-wave ($m = 0$) and even-wave ($m = \pm 1$) sectors with respective solutions given by

$$T_o^{-1} \equiv \left(\frac{1}{\pi a_\perp^2} T_{\text{q1D}}^{(0)}(E_{\text{rel}}) \right)^{-1}$$
$$= \frac{2\mu}{2} \left[\frac{a_\perp^2}{6} \left(\frac{1}{V_{\text{3D}}} + \frac{2\mu E_{\text{rel}}}{R_{\text{3D}}} \right) - \frac{2}{a_\perp} \zeta \left(-\frac{1}{2}, -\mathcal{E}_0 - i\varepsilon \right) \right], \quad (A5)$$

$$T_e^{-1} \equiv \left(\frac{2}{\pi a_\perp^4} T_{\text{q1D}}^{(\pm 1)}(E_{\text{rel}}) \right)^{-1}$$
$$= \frac{2\mu}{2} \left[\frac{a_\perp^4}{12} \left(\frac{1}{V_{\text{3D}}} + \frac{2\mu E_{\text{rel}}}{R_{\text{3D}}} \right) + \frac{a_\perp}{2} \zeta \left(-\frac{1}{2}, -\mathcal{E}_1 - i\varepsilon \right) \right.$$
$$\left. + \frac{a_\perp}{2} \frac{E_{\text{rel}}}{2\omega_\perp} \zeta \left(\frac{1}{2}, -\mathcal{E}_1 - i\varepsilon \right) \right]. \quad (A6)$$

Here, $\zeta(s, x)$ is the Hurwitz zeta function, ε is an infinitesimally small positive quantity, and $\mathcal{E}_m = [E_{\text{rel}} - (|m| + 1)\omega_\perp]/2\omega_\perp = (ka_\perp/2)^2$. We have also defined the appropriate renormalized q1D scattering T matrices T_o (odd wave) and T_e (even wave) that have a direct correspondence with scattering T matrices in true 1D systems.

The resonance condition for q1D scattering is $a_o^{-1} = 0$ for the odd-wave case or $a_e = 0$ for the even-wave case. In the low-energy regime $\mathcal{E}_m \ll 1$, the bound-state energies for the odd-wave and even-wave sectors are given by

$$E_{B,o} = \omega_\perp - \frac{\kappa_o^2}{2\mu} \quad \text{with} \quad \kappa_o = \frac{1}{a_o} - \kappa_o^2 r_o \quad (A7)$$

and

$$E_{B,e} = 2\omega_\perp - \frac{\kappa_e^2}{2\mu} \quad \text{with} \quad \frac{1}{\kappa_e} = a_e + \kappa_e^2 r_e, \quad (A8)$$

where $\kappa_o > 0$ and $\kappa_e > 0$ are the odd-wave and even-wave bound-state wave numbers, respectively. The binding energies are consistent with true 1D calculations in the shallow-dimer limit ($\kappa a_\perp \ll 1$): for repulsive odd waves, $a_o > 0$, $\omega_\perp - E_{B,o} \approx 1/(2\mu a_o^2)$, and for attractive even waves, $a_e > 0$, $2\omega_\perp - E_{B,e} \approx 1/(2\mu a_e^2)$.

APPENDIX B: RF SPECTRAL FORM IN THE q1D REGIME

Here, we derive the analytic expressions for the rf transition rate $\Gamma(\omega)$ at high frequency, taking into account the multiple transverse excited bands. From standard arguments [108], the dominant contribution to the rf transfer rate at high frequencies is determined by the short-range part of the many-body wave function, which is essentially the same as the two-body case at zero energy, apart from a normalization constant (which we will introduce as γ_0 or γ_1 momentarily) that depends on the many-body physics. Since we have evaluated the two-body

T matrix exactly for cylindrically symmetric q1D scattering in Sec. III A, we can evaluate Eq. (13) in the high-frequency limit [45,83], which gives the exact functional dependencies of $\Gamma(\omega)$ apart from overall constants that characterize the many-body states. We find that the rf transfer rate can be written as $\Gamma(\omega) = \sum_{m=-1}^{+1} \Gamma^{(m)}(\omega)$, with

$$\Gamma^{(0)}(\omega) = \gamma_0 \frac{\Omega^2}{8\pi} \frac{(2\omega_\perp)^{3/2}}{\omega^2}$$
$$\times \sum_{\mathcal{N}=0}^{\infty} \left(\frac{\omega}{2\omega_\perp} - \mathcal{N}\right)^{1/2} \theta\left(\frac{\omega}{2\omega_\perp} - \mathcal{N}\right) \quad \text{(B1)}$$

and

$$\Gamma^{(\pm 1)}(\omega) = \gamma_1 \frac{\Omega^2}{8\pi} \frac{(2\omega_\perp)^{3/2}}{\omega^2}$$
$$\times \sum_{\mathcal{N}=0}^{\infty} (\mathcal{N}+1)\left(\frac{\omega}{2\omega_\perp} - \mathcal{N}\right)^{-1/2} \theta\left(\frac{\omega}{2\omega_\perp} - \mathcal{N}\right).$$
$$\text{(B2)}$$

Equations (B1) and (B2) are valid for large positive detuning $\omega \gg E_F$. For both $\Gamma^{(0)}(\omega)$ and $\Gamma^{(\pm 1)}(\omega)$, the sum over $\mathcal{N}$ represents the contributions from all radially excited states. The physical interpretation of this expression is similar to Eqs. (14) and (15) given in the main text but now generalized: the step function $\theta(\omega/2\omega_\perp - \mathcal{N})$ indicates the opening of the transverse band for which the rf photon energy exceeds the energy difference to the $\mathcal{N}$th scattering continuum.

This calculation clarifies the condition in which true-1D scaling in the rf spectrum is observed. Specifically, the 1D odd- and even-wave contact relations apply when $|\omega| < 2\omega_\perp$, a regime in which only the continuum states with $\mathcal{N} = 0$ are relevant. In this case,

$$\Gamma^{(0)}(\omega) = \gamma_0 \Omega^2 \frac{2\omega_\perp}{8\pi} \frac{1}{\omega^{3/2}}, \quad \text{(B3)}$$

$$\Gamma^{(\pm 1)}(\omega) = \gamma_1 \Omega^2 \frac{(2\omega_\perp)^2}{8\pi} \frac{1}{\omega^{5/2}}. \quad \text{(B4)}$$

These two relations should be identified with the expressions for $\Gamma(\omega)$ from the exact 1D odd-wave [27] and even-wave scattering calculations:

$$\Gamma^{(0)}(\omega) = \frac{\Omega^2}{2\omega^{3/2}} C_o \quad \text{and} \quad \Gamma^{(\pm 1)}(\omega) = \frac{\Omega^2}{2\omega^{5/2}} C_e, \quad \text{(B5)}$$

where C_o and C_e are the 1D odd-wave and even-wave contacts, respectively. We thus identify γ_0 and γ_1 as

$$\gamma_0 = \frac{4\pi}{2\omega_\perp} C_o \quad \text{and} \quad \gamma_1 = \frac{4\pi}{(2\omega_\perp)^2} C_e. \quad \text{(B6)}$$

Using these relations in Eqs. (B1) and (B2), we obtain the limiting forms in Eqs. (14)–(17) in the main text, which are relevant to q1D physics. However, in the limit $\omega \to \infty$, increasingly shorter length scales are probed as the continuum final states of higher transverse bands are made available, eventually approaching the 3D limit; this behavior is also present in Eqs. (B1) and (B2). Replacing the sum over transverse radial states with an integral, one reproduces the correct leading-order $\omega^{-1/2}$ rf spectral law for a *p*-wave Fermi gas in 3D. A related discussion of the q1D momentum distribution is presented in Ref. [109].

APPENDIX C: FINAL-STATE EFFECTS IN EVEN-WAVE SPECTROSCOPY

The ideal scenario of rf spin-flip spectroscopy is that an atom is transferred from an interacting state to a non-interacting state. This is a good approximation when interactions in the initial spin state are near resonant, and the final states at the same magnetic field are far from resonance. In the situation probed in our experiments, atoms are spin flipped from $|b\rangle$ to $|c\rangle$, so bb *p*-wave interactions should be large compared to bc *p*-wave interactions. Coupled-channel calculations indicate that the z-dimer bc *p*-wave Feshbach resonance is located at $B_0 = 217.12$ G, with a scattering volume that can be parametrized as $V_{bc}(B)/V_{bg} = 1 - \Delta/(B - B_0)$, with $V_{bg} = (-107.95 a_0)^3$ and $\Delta = -8.98$ G, where a_0 is the Bohr radius. This yields a zero crossing near 208 G, such that V_{bc} is below its background value in the range of fields across which we measure q1D contacts, typically 200 G–205 G, and can hence be considered as weakly interacting in this regime.

For even-wave spectroscopy, adding final-state effects to Eq. (17), the relation between Γ and C_e is

$$\lim_{\omega \to \infty} \Gamma(\omega) = \frac{\Omega^2}{2\sqrt{\hbar m}} \frac{C_e}{\omega^{5/2}} \frac{(a_e - a'_e - m\omega(r_e - r'_e)/\hbar)^2}{(m\omega r'_e/\hbar - a'_e)^2 + (m\omega/\hbar)^{-1}}, \quad \text{(C1)}$$

where a'_e and r'_e are the 1D scattering parameters for the bc channel. Equation (C1) predicts a deviation of $\Gamma(\omega)$ from its asymptotic form; however, within the range of frequency and scattering parameters relevant to the experiment, it does not explain the deviation of the even-wave rf spectrum from the $-5/2$ scaling shown in Fig. 7.

In our regime of interest, Eq. (C1) can be approximated as

$$\lim_{\omega \to \infty} \Gamma(\omega) = \frac{\Omega^2}{2\sqrt{\hbar m}} \frac{C_e}{\omega^{5/2}} \frac{(a_e - a'_e)^2}{a'^2_e}. \quad \text{(C2)}$$

This allows us to bound the final-state effects to corrections between 0.90 and 1.05 using V_{bc} and a typical value of R_{3D} in the field and depth range used in Fig. 8. Since this is less than the scatter of the experimental data, we can safely neglect final-state effects.

APPENDIX D: HIGH-TEMPERATURE EXPANSION FOR THE ODD- AND EVEN-WAVE CONTACTS

In the high-temperature regime of small fugacity, $z \ll 1$, analytic forms of the many-body contact can be found from a virial expansion [32,110–113]. Although we explore systems with T comparable to T_F, the high-temperature approximation provides a qualitative comparison between theory and experiment with no adjustable parameters. Here, we consider a homogeneous 1D system with length L, uniform density n, and total number $N = Ln$. For comparison to experimental data, we use a correction for inhomogeneity as described in Appendix F.

1. Odd-wave contact

The high-temperature calculation of the odd-wave contact comes from a two-channel model of interacting atoms and closed-channel molecules [32]. For weak attractive interactions $|a_o|/\Lambda_T \ll 1$ and $a_o < 0$,

$$C_o = \frac{2\pi\hbar^2 N n a_o^2}{m\Lambda_T^2}\left[1 - 6\pi\frac{a_o r_o}{\Lambda_T^2}\right], \qquad (\text{D1})$$

where $\Lambda_T = (2\pi\hbar^2\beta/m)^{1/2}$ is the single-particle thermal de Broglie wavelength. As assumed in Appendix F, the contact is Nn times a function of T, a_o, and r_o. A convenient form uses k_F and E_F of the central tube as reference values:

$$\frac{C_o}{N} = \frac{\hbar^2 k_F^3 \tilde{T} a_o^2}{2\pi m}\left(1 + \frac{3}{2}k_F^2 r_o a_o \tilde{T}\right), \qquad (\text{D2})$$

where we have used $\Lambda_T^{-2} = \tilde{T}k_F^2/4\pi$ and $k_F = \pi n$.

2. Even-wave contact

The calculation technique for the even-wave contact follows the high-temperature treatment for odd waves [32], i.e., using a two-channel model of spin-half fermions coupled to closed-channel molecules to evaluate the contacts for arbitrary interaction strengths. To model the anisotropic nature of the interactions and the trapping potential, we assume that the x and z resonances are independent 1D systems. The expression for the contact $C_e^{x,z}$ has a contribution from the scattering continuum $(C_e|_{at})$ and a contribution from the two-body bound state $(C_e|_{mol})$. Omitting the direction label (x, z), these two terms are

$$C_e|_{at} = N_1 n p_0 \int_0^\infty du\, \frac{2\pi^{-1/2}u^{1/2}e^{-u}}{\frac{mu}{\hbar^2}\left(a_e - \frac{mu}{\hbar^2\beta}r_e\right)^2 + \beta}, \qquad (\text{D3})$$

where the integration variable is dimensionless, $p_0 \equiv N_0/(N_0 + N_1)$ is the population fraction of ground-band atoms, and

$$C_e|_{mol} \approx N_1 n p_0 \frac{\hbar^2}{m}\frac{\sqrt{2}\Lambda_T\theta(a_e)}{r_e + |a_e|^3/2}e^{\beta\hbar^2/(ma_e^2)}, \qquad (\text{D4})$$

where $\theta()$ is the Heaviside step function. Note that in Eq. (D4), we use the shallow-dimer limit instead of the full Eq. (A8), which is a good approximation in the $k_F a_e > 2$ range for which the high-temperature C_e is considered in Fig. 8. Just like the odd-wave case, the even-wave contact is a function of Nn but now multiplied by the fraction in each band.

Scaling by k_F and E_F of the central tube, the sum of these contributions is

$$\frac{C_e}{N_1} = \frac{2p_0\hbar^2 k_F^3}{\pi^{3/2}m}\left\{\frac{\sqrt{2}\pi e^{2/(k_F^2 a_e^2 \tilde{T})}}{k_F^3 r_e + |k_F a_e|^3/2}\tilde{T}^{-1/2}\right.$$
$$\left. + \int_0^\infty du\, \frac{u^{1/2}e^{-u}}{u(k_F a_e - u k_F^3 r_e \tilde{T}/2)^2 + 2\tilde{T}^{-1}}\right\}, \qquad (\text{D5})$$

which is plotted in Fig. 8. In the weakly interacting limit, the even-wave contacts are given by

$$\frac{C_e}{N_1} \approx \frac{2p_0\hbar^2 k_F}{\pi m}a_e^{-2}. \qquad (\text{D6})$$

In the resonantly interacting limit, the high-temperature theory breaks down, as the binding energy proportional to $1/a_e^2$ quickly exceeds the temperature, invalidating the high-temperature assumption.

APPENDIX E: RF SPECTROSCOPY WITH VARIABLE BAND POPULATIONS

The odd- and even-wave contacts are extensive quantities that are proportional to population in the relevant bands at high temperature. We are able to manipulate band populations with two types of lattice modulations—amplitude modulation (AM) and frequency modulation (FM). In this appendix, we show their effects on the measured contacts.

Figure 9(a) illustrates AM and its primary effect on band populations. Due to anharmonicity of the lattice, the resonant frequency for transfer between the first and third excited states is lower than for transfer between the ground state and the second excited state. Since atoms in the third band leave the trap, this process distills the ground band.
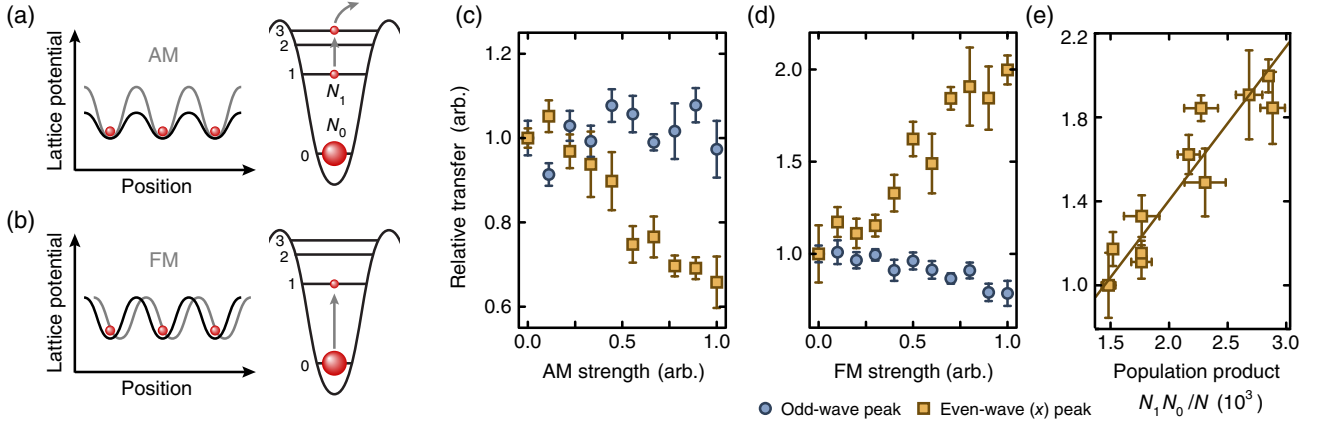
FIG. 9. Correlation of transfer with modulation type and strength. (a) Amplitude modulation of the lattice potential causing a single-particle first-to-third transition that removes atoms from the first excited band. (b) Frequency modulation causing a single-particle zero-to-first transition to populate the excited band while also depleting the ground band. (c) Number of atoms transferred to the probe state from $\tilde{\omega}/2\pi = 50$ kHz for $40\,E_R$ confinement with varying AM strength. There is no significant change in transfer at the odd-wave peak (199.25 G). Less transfer is noticed at the even-wave (x) peak (199.75 G). Transfer is plotted relative to the transfer with no modulation. (d) Transferred atoms for various frequency modulations. A slight decrease in transfer for the odd-wave peak is seen as atoms are transferred out of the ground band. Transfer is increased for the even-wave peak. (e) Transfer at even-wave peak plotted versus the population product excited- and ground-state populations (see text) divided by N_{tot} and compared to a linear fit. All error bars in this figure represent one standard deviation.

Phase modulation of the optical standing wave is implemented experimentally by FM of the light, which creates a time-dependent displacement of local potential minima where atoms are trapped, due to the optical propagation to the retroreflecting mirror and back. Figure 9(b) illustrates this local position displacement of the lattice potential. Unlike AM, phase modulation provides the necessary parity-breaking time-dependent gradient to transfer atoms from the ground band to the first excited band.

The effects of AM on the odd- and even-wave contacts are shown in Fig. 9(c). Here, circles and squares report Γ at magnetic fields near the odd-wave and even-wave peaks, respectively, proportional to the (extensive) contact. We see that increasing AM strength has no noticeable trend in Γ at the odd-wave peak, which is consistent with odd-wave correlations being due to scattering between ground-band atoms. At the even-wave peak, the decrease of Γ with AM is also consistent with even-wave correlations being proportional to the excited-band population.

Similarly, the effect of FM is shown in Fig. 9(d). Since FM modulates atoms from the ground band to the excited band, one might expect an equal change in the strength of correlations for odd and even waves. Instead, we observe that increasing modulation strength only slightly decreases transfer at the odd-wave peak and causes comparatively large increases in transfer for the even-wave peak. Thus, we remark that the relatively equal weights for the peaks seen in Fig. 2(b) are coincidental for the nearly 15% of excited-band atoms populated by our multiband loading procedure.

Figure 9(e) demonstrates how transfer at the even-wave peak is correlated with the product of ground- and excited-state atom populations, counted in band-mapped time-of-flight imaging. A linear fit of the measurements has a zero crossing within uncertainty of zero and a reduced χ^2 of 1.07. This measurement provides us with the confidence to attribute the transfer seen at the even-wave peaks to a measure of correlations between ground- and excited-band atoms.

APPENDIX F: INHOMOGENEOUS AVERAGING

The theoretical description of atom-atom correlations throughout this paper assumes a single q1D system with a homogeneous atomic density. Our experimental measurements average across two types of inhomogeneities: the density profile within a single tube, and tube-to-tube variation in N. In the high-temperature limit, $C_{hom}/N n_{1D}$ for a uniform-density gas is solely a function of temperature, scattering parameters, and confinement strength (see Appendix D), i.e., variables that are uniform across our ensemble. We can thus account for inhomogeneities by separating out the dependence of contact on atom number and density as

$$\langle C \rangle_{obs} = \langle N n_{1D} \rangle \frac{C_{hom}}{N n_{1D}}, \qquad (F1)$$

where $\langle Nn \rangle$ is an average across the ensemble.

The inhomogeneity within each tube is treated with a local density approximation: that each differential length dy contributes $n_{1D}^2(y)dy$ to $N n_{1D}$. In the high-temperature limit, the density distribution is given by a Maxwell-Boltzmann distribution, so

$$\langle Nn_{1D}\rangle_{\text{tube}} = \int n_{1D}^2(y)dy = (4\pi)^{-1/2}N^2/R_T, \quad \text{(F2)}$$

where $R_T = (k_BT/m\omega_y^2)^{1/2}$ is the thermal length of the cloud. By comparison, the peak 1D density is $(2\pi)^{-1/2}N/R_T$, such that $\langle Nn_{1D}\rangle_{\text{tube}} = Nn_{\text{pk}}/\sqrt{2}$.

We model the distribution of q1D ensembles by assuming that the transfer between a 3D Fermi gas and an array of tubes is isentropic. This approach neglects the fraction of atoms that appear in higher bands since edges of the Brillouin zone cannot be adiabatic. This transfer occurs during the first t_{ramp} phase of Fig. 1(b)(i), up to a modest depth ($V_L < 10E_R$). The density of states of the low-depth array is a convolution of a harmonic-lattice density of states $\rho(\epsilon) = 2\sqrt{E_R}/\pi\hbar\omega_\perp\sqrt{\epsilon}$ [114,115] in the x and z directions, with a 1D harmonic oscillator $\rho(\epsilon) = 1/\hbar\omega_y$ along the tube, where ϵ is energy. We find the chemical potential and temperature of the transformed tube array by imposing entropy and number conservation between the preloaded gas to the array of tubes. After this loading phase, energy and particle transport between the tubes are suppressed as the lattice depths increase to their final values. Including a -20% corrective factor for atom loss observed in round-trip loading calibrations, we find the number and temperature of the central tube to be $N^* \approx 30$ and $\tilde{T} \approx 0.8$ for typical conditions, where $\tilde{T} = k_BT/E_F$; here and below, we use N^* to define a reference value of the 1D Fermi energy E_F. The atom-number distribution of this adiabatic loading model is compared to a diabatic model in which the initial 3D density distribution is partitioned into a square array of parallelepipeds. In both models, the distribution of N is found to be roughly uniform: i.e., the number of tubes that have near-peak atom number is the same as the number of tubes that have only one atom.

We define a distribution function w_N of atom number that satisfies $\sum_N w_N = M$, where M is the total number of tubes, and $\sum_N w_N N = N_{\text{tot}}$. Without a dispersion in atom number, each of the M tubes would have N^* atoms, so that $N_{\text{tot}} = N^*M$, and the distribution function would be $w_N = N_{\text{tot}}\delta_{N,N^*}/N^*$. Instead, in the distribution found by these loading models, w_N^{exp} is approximately constant between $N = 1$ and $N = N^*$, and zero otherwise. This gives

$$N_{\text{tot}} = w_N^{\text{exp}}\sum_{N=1}^{N^*}N = \frac{1}{2}(N^*+1)N^*w_N^{\text{exp}}. \quad \text{(F3)}$$

We can rearrange this expression to find $w_N^{\text{exp}} = 2N_{\text{tot}}/[(N^*+1)N^*]$ for $1 \le N \le N^*$. Since the contact is proportional to N^2 in the high-temperature limit [see Eq. (F2)], the ratio of the contacts in these two cases is given by

$$\frac{\langle N^2\rangle^{\text{exp}}}{(N^*)^2} = \frac{1}{N_{\text{tot}}N^*}\sum_{N=1}^{N^*}w_N^{\text{exp}}N^2 = \frac{1+2N^*}{3N^*}, \quad \text{(F4)}$$

which approaches $2/3$ for large N^*.

Combining the intratube and intertube inhomogeneity effects yields a correction in the estimated value of the contact,

$$\frac{\langle C_{\text{tube}}\rangle^{\text{exp}}}{C_{\text{hom}}} = \frac{2}{3}\sqrt{\frac{\pi}{8}}\tilde{T}^{-1/2}. \quad \text{(F5)}$$

The theoretical curves shown in Figs. 5 and 8 use the uniform-gas prediction multiplied by this correction, which is about 0.4 for typical loading parameters.

---

[1] R. Prange, M. Cage, K. Klitzing, S. Girvin, A. Chang, F. Duncan, M. Haldane, R. Laughlin, A. Pruisken, and D. Thouless, *The Quantum Hall Effect*, Graduate Texts in Contemporary Physics (Springer, New York, 2012).

[2] S. E. Barrett, G. Dabbagh, L. N. Pfeiffer, K. W. West, and R. Tycko, *Optically Pumped NMR Evidence for Finite-Size Skyrmions in GaAs Quantum Wells Near Landau Level Filling $\nu = 1$*, Phys. Rev. Lett. **74**, 5112 (1995).

[3] E. H. Aifer, B. B. Goldberg, and D. A. Broido, *Evidence of Skyrmion Excitations about $\nu = 1$ in n-Modulation-Doped Single Quantum Wells by Interband Optical Transmission*, Phys. Rev. Lett. **76**, 680 (1996).

[4] J. Vijayan, P. Sompet, G. Salomon, J. Koepsell, S. Hirthe, A. Bohrdt, F. Grusdt, I. Bloch, and C. Gross, *Time-Resolved Observation of Spin-Charge Deconfinement in Fermionic Hubbard Chains*, Science **367**, 186 (2020).

[5] R. Senaratne, D. Cavazos-Cavazos, S. Wang, F. He, Y.-T. Chang, A. Kafle, H. Pu, X.-W. Guan, and R. Hulet, *Spin-Charge Separation in a One-Dimensional Fermi Gas with Tunable Interactions*, Science **376**, 1305 (2022).

[6] M. Olshanii, *Atomic Scattering in the Presence of an External Confinement and a Gas of Impenetrable Bosons*, Phys. Rev. Lett. **81**, 938 (1998).

[7] T. Giamarchi, *Theory for 1D Quantum Materials Tested with Cold Atoms and Superconductors*, Physics **10**, 115 (2017).

[8] F. Møller, C. Li, I. Mazets, H.-P. Stimming, T. Zhou, Z. Zhu, X. Chen, and J. Schmiedmayer, *Extension of the Generalized Hydrodynamics to the Dimensional Cross-over Regime*, Phys. Rev. Lett. **126**, 090602 (2021).

[9] T. Bergeman, M. G. Moore, and M. Olshanii, *Atom-Atom Scattering under Cylindrical Harmonic Confinement: Numerical and Analytic Studies of the Confinement In-duced Resonance*, Phys. Rev. Lett. **91**, 163201 (2003).

[10] G. Moore, T. Bergeman, and M. Olshanii, *Scattering in Tight Atom Waveguides*, J. Phys. IV **116**, 69 (2004).

[11] J. I. Kim, J. Schmiedmayer, and P. Schmelcher, *Quantum Scattering in Quasi-One-Dimensional Cylindrical Con-finement*, Phys. Rev. A **72**, 042711 (2005).

[12] V. A. Yurovsky, *Feshbach Resonance Scattering under Cylindrical Harmonic Confinement*, Phys. Rev. A **71,** 012709 (2005).

[13] P. Naidon, E. Tiesinga, W. F. Mitchell, and P. S. Julienne, *Effective-Range Description of a Bose Gas under Strong One- or Two-Dimensional Confinement*, New J. Phys. **9,** 19 (2007).

[14] V. Dunjko, M. G. Moore, T. Bergeman, and M. Olshanii, Confinement-Induced Resonances, in *Advances in Atomic, Molecular, and Optical Physics*, Vol. 60, edited by E. Arimondo, P. Berman, and C. Lin (Academic Press, New York, 2011), pp. 461–510.

[15] T. Kristensen and L. Pricoupenko, *Ultracold-Atom Collisions in Atomic Waveguides: A Two-Channel Analysis*, Phys. Rev. A **91,** 042703 (2015).

[16] K. Günter, T. Stöferle, H. Moritz, M. Köhl, and T. Esslinger, *p-Wave Interactions in Low-Dimensional Fermionic Gases*, Phys. Rev. Lett. **95,** 230401 (2005).

[17] M. Waseem, Z. Zhang, J. Yoshida, K. Hattori, T. Saito, and T. Mukaiyama, *Creation of p-Wave Feshbach Molecules in Selected Angular Momentum States Using an Optical Lattice*, J. Phys. B **49,** 204001 (2016).

[18] Y.-T. Chang, R. Senaratne, D. Cavazos-Cavazos, and R. G. Hulet, *Collisional Loss of One-Dimensional Fermions Near a p-Wave Feshbach Resonance*, Phys. Rev. Lett. **125,** 263402 (2020).

[19] A. S. Marcum, F. R. Fonta, A. M. Ismail, and K. M. O'Hara, *Suppression of Three-Body Loss Near a p-Wave Resonance Due to Quasi-1D Confinement*, arXiv: 2007.15783.

[20] B. E. Granger and D. Blume, *Tuning the Interactions of Spin-Polarized Fermions Using Quasi-One-Dimensional Confinement*, Phys. Rev. Lett. **92,** 133202 (2004).

[21] K. Kanjilal and D. Blume, *Nondivergent Pseudopotential Treatment of Spin-Polarized Fermions under One- and Three-Dimensional Harmonic Confinement*, Phys. Rev. A **70,** 042709 (2004).

[22] M. Girardeau, H. Nguyen, and M. Olshanii, *Effective Interactions, Fermi-Bose Duality, and Ground States of Ultracold Atomic Vapors in Tight de Broglie Waveguides*, Opt. Commun. **243,** 3 (2004).

[23] L. Pricoupenko, *Resonant Scattering of Ultracold Atoms in Low Dimensions*, Phys. Rev. Lett. **100,** 170404 (2008).

[24] B. Heß, P. Giannakeas, and P. Schmelcher, *Energy-Dependent ℓ-Wave Confinement-Induced Resonances*, Phys. Rev. A **89,** 052716 (2014).

[25] T.-Y. Gao, S.-G. Peng, and K. Jiang, *Two-Body State with p-Wave Interaction in a One-Dimensional Waveguide under Transversely Anisotropic Confinement*, Phys. Rev. A **91,** 043622 (2015).

[26] S. Saeidian, V. S. Melezhik, and P. Schmelcher, *Shifts and Widths of p-Wave Confinement Induced Resonances in Atomic Waveguides*, J. Phys. B **48,** 155301 (2015).

[27] X. Cui, *Universal One-Dimensional Atomic Gases Near Odd-Wave Resonance*, Phys. Rev. A **94,** 043636 (2016).

[28] X. Cui and H. Dong, *High-Momentum Distribution with a Sub-leading k^{-3} Tail in Odd-Wave Interacting One-Dimensional Fermi Gases*, Phys. Rev. A **94,** 063650 (2016).

[29] Y. Sekino, S. Tan, and Y. Nishida, *Comparative Study of One-Dimensional Bose and Fermi Gases with Contact Interactions from the Viewpoint of Universal Relations for Correlation Functions*, Phys. Rev. A **97,** 013621 (2018).

[30] L. Pan, S. Chen, and X. Cui, *Many-Body Stabilization of a Resonant p-Wave Fermi Gas in One Dimension*, Phys. Rev. A **98,** 011603(R) (2018).

[31] X. Yin, X.-W. Guan, Y. Zhang, H. Su, and S. Zhang, *Momentum Distribution and Contacts of One-Dimensional Spinless Fermi Gases with an Attractive p-Wave Interaction*, Phys. Rev. A **98,** 023605 (2018).

[32] J. Maki, *Thermodynamic Contacts and Breathing-Mode Physics of One-Dimensional p-Wave Fermi Gases in the High-Temperature Limit*, Phys. Rev. A **104,** 063314 (2021).

[33] J. Maki and S. Zhang, *Viscous Flow in a One-Dimensional Spin-Polarized Fermi Gas: The Role of Integrability on Viscosity*, Phys. Rev. A **107,** 013310 (2023).

[34] L. Zhou and X. Cui, *Stretching p-Wave Molecules by Transverse Confinements*, Phys. Rev. A **96,** 030701(R) (2017).

[35] F. Fonta and K. M. O'Hara, *Experimental Conditions for Obtaining Halo p-Wave Dimers in Quasi-One-Dimension*, Phys. Rev. A **102,** 043319 (2020).

[36] D. V. Kurlov and G. V. Shlyapnikov, *Two-Body Relaxation of Spin-Polarized Fermions in Reduced Dimensionalities Near a p-Wave Feshbach Resonance*, Phys. Rev. A **95,** 032710 (2017).

[37] C. A. Regal, C. Ticknor, J. L. Bohn, and D. S. Jin, *Tuning p-Wave Interactions in an Ultracold Fermi Gas of Atoms*, Phys. Rev. Lett. **90,** 053201 (2003).

[38] J. Zhang, E. G. M. van Kempen, T. Bourdel, L. Khaykovich, J. Cubizolles, F. Chevy, M. Teichmann, L. Tarruell, S. J. J. M. F. Kokkelmans, and C. Salomon, *p-Wave Feshbach Resonances of Ultracold ^{6}Li*, Phys. Rev. A **70,** 030702(R) (2004).

[39] C. H. Schunck, M. W. Zwierlein, C. A. Stan, S. M. F. Raupach, W. Ketterle, A. Simoni, E. Tiesinga, C. J. Williams, and P. S. Julienne, *Feshbach Resonances in Fermionic ^{6}Li*, Phys. Rev. A **71,** 045601 (2005).

[40] F. Chevy, E. G. M. van Kempen, T. Bourdel, J. Zhang, L. Khaykovich, M. Teichmann, L. Tarruell, S. J. J. M. F. Kokkelmans, and C. Salomon, *Resonant Scattering Properties Close to a p-Wave Feshbach Resonance*, Phys. Rev. A **71,** 062710 (2005).

[41] Y. Inada, M. Horikoshi, S. Nakajima, M. Kuwata-Gonokami, M. Ueda, and T. Mukaiyama, *Collisional Properties of p-Wave Feshbach Molecules*, Phys. Rev. Lett. **101,** 100401 (2008).

[42] S. Tan, *Energetics of a Strongly Correlated Fermi Gas*, Ann. Phys. (N.Y.) **323,** 2952 (2008).

[43] S. Tan, *Large Momentum Part of a Strongly Correlated Fermi Gas*, Ann. Phys. (N.Y.) **323,** 2971 (2008).

[44] S. Tan, *Generalized Virial Theorem and Pressure Relation for a Strongly Correlated Fermi Gas*, Ann. Phys. (N.Y.) **323,** 2987 (2008).

[45] E. Braaten and L. Platter, *Exact Relations for a Strongly Interacting Fermi Gas from the Operator Product Expansion*, Phys. Rev. Lett. **100,** 205301 (2008).

[46] E. Braaten, D. Kang, and L. Platter, *Universal Relations for a Strongly Interacting Fermi Gas Near a Feshbach Resonance*, Phys. Rev. A **78**, 053606 (2008).

[47] F. Werner, L. Tarruell, and Y. Castin, *Number of Closed-Channel Molecules in the BEC-BCS Crossover*, Euro. Phys. J. B **68**, 401 (2009).

[48] S. Zhang and A. J. Leggett, *Universal Properties of the Ultracold Fermi Gas*, Phys. Rev. A **79**, 023601 (2009).

[49] E. Braaten, D. Kang, and L. Platter, *Short-Time Operator Product Expansion for rf Spectroscopy of a Strongly Interacting Fermi Gas*, Phys. Rev. Lett. **104**, 223004 (2010).

[50] E. Braaten, *Universal Relations for Fermions with Large Scattering Length*, in *The BCS-BEC Crossover and the Unitary Fermi Gas*, edited by W. Zwerger (Springer, Berlin, 2012), pp. 193–231.

[51] F. Werner and Y. Castin, *General Relations for Quantum Gases in Two and Three Dimensions: Two-Component Fermions*, Phys. Rev. A **86**, 013626 (2012).

[52] F. Werner and Y. Castin, *General Relations for Quantum Gases in Two and Three Dimensions. II. Bosons and Mixtures*, Phys. Rev. A **86**, 053633 (2012).

[53] S. M. Yoshida and M. Ueda, *Universal High-Momentum Asymptote and Thermodynamic Relations in a Spinless Fermi Gas with a Resonant p-Wave Interaction*, Phys. Rev. Lett. **115**, 135303 (2015).

[54] Z. Yu, J. H. Thywissen, and S. Zhang, *Universal Relations for a Fermi Gas Close to a p-Wave Interaction Resonance*, Phys. Rev. Lett. **115**, 135304 (2015).

[55] C. Luciuk, S. Trotzky, S. Smale, Z. Yu, S. Zhang, and J. H. Thywissen, *Evidence for Universal Relations Describing a Gas with p-Wave Interactions*, Nat. Phys. **12**, 599 (2016).

[56] M. He, S. Zhang, H. M. Chan, and Q. Zhou, *Concept of a Contact Spectrum and Its Applications in Atomic Quantum Hall States*, Phys. Rev. Lett. **116**, 045301 (2016).

[57] S.-G. Peng, X.-J. Liu, and H. Hu, *Large-Momentum Distribution of a Polarized Fermi Gas and p-Wave Contacts*, Phys. Rev. A **94**, 063651 (2016).

[58] M. Olshanii and V. Dunjko, *Short-Distance Correlation Properties of the Lieb-Liniger System and Momentum Distributions of Trapped One-Dimensional Atomic Gases*, Phys. Rev. Lett. **91**, 090401 (2003).

[59] M. Barth and W. Zwerger, *Tan Relations in One Dimension*, Ann. Phys. (N.Y.) **326**, 2544 (2011).

[60] W.-B. He, Y.-Y. Chen, S. Zhang, and X.-W. Guan, *Universal Properties of Fermi Gases in One Dimension*, Phys. Rev. A **94**, 031604(R) (2016).

[61] J. T. Stewart, J. P. Gaebler, T. E. Drake, and D. S. Jin, *Verification of Universal Relations in a Strongly Interacting Fermi Gas*, Phys. Rev. Lett. **104**, 235301 (2010).

[62] E. D. Kuhnle, H. Hu, X.-J. Liu, P. Dyke, M. Mark, P. D. Drummond, P. Hannaford, and C. J. Vale, *Universal Behavior of Pair Correlations in a Strongly Interacting Fermi Gas*, Phys. Rev. Lett. **105**, 070402 (2010).

[63] S. Hoinka, M. Lingham, K. Fenech, H. Hu, C. J. Vale, J. E. Drut, and S. Gandolfi, *Precise Determination of the Structure Factor and Contact in a Unitary Fermi Gas*, Phys. Rev. Lett. **110**, 055305 (2013).

[64] B. Fröhlich, M. Feld, E. Vogt, M. Koschorreck, M. Köhl, C. Berthod, and T. Giamarchi, *Two-Dimensional Fermi Liquid with Attractive Interactions*, Phys. Rev. Lett. **109**, 130403 (2012).

[65] C. Luciuk, S. Smale, F. Böttcher, H. Sharum, B. A. Olsen, S. Trotzky, T. Enss, and J. H. Thywissen, *Observation of Quantum-Limited Spin Transport in Strongly Interacting Two-Dimensional Fermi Gases*, Phys. Rev. Lett. **118**, 130405 (2017).

[66] J. P. Gaebler, J. T. Stewart, J. L. Bohn, and D. S. Jin, *p-Wave Feshbach Molecules*, Phys. Rev. Lett. **98**, 200403 (2007).

[67] J. Fuchs, C. Ticknor, P. Dyke, G. Veeravalli, E. Kuhnle, W. Rowlands, P. Hannaford, and C. J. Vale, *Binding Energies of ^{6}Li p-Wave Feshbach Molecules*, Phys. Rev. A **77**, 053616 (2008).

[68] D. J. M. Ahmed-Braun, K. G. Jackson, S. Smale, C. J. Dale, B. A. Olsen, S. J. J. M. F. Kokkelmans, P. S. Julienne, and J. H. Thywissen, *Probing Open- and Closed-Channel p-Wave Resonances*, Phys. Rev. Res. **3**, 033269 (2021).

[69] H. W. Hammer and D. Lee, *Causality and Universality in Low-Energy Quantum Scattering*, Phys. Lett. B **681**, 500 (2009).

[70] H. W. Hammer and D. Lee, *Causality and the Effective Range Expansion*, Ann. Phys. (N.Y.) **325**, 2212 (2010).

[71] E. Braaten, P. Hagen, H. W. Hammer, and L. Platter, *Renormalization in the Three-Body Problem with Resonant p-Wave Interactions*, Phys. Rev. A **86**, 012711 (2012).

[72] C. A. Bertulani, H.-W. Hammer, and U. van Kolck, *Effective Field Theory for Halo Nuclei: Shallow p-Wave States*, Nucl. Phys. **A712**, 37 (2002).

[73] P. Bedaque, H.-W. Hammer, and U. van Kolck, *Narrow Resonances in Effective Field Theory*, Phys. Lett. B **569**, 159 (2003).

[74] K. B. Gubbels and H. T. C. Stoof, *Theory for p-Wave Feshbach Molecules*, Phys. Rev. Lett. **99**, 190406 (2007).

[75] J. Maki and S. Zhang, *Role of Effective Range in the Bulk Viscosity of Resonantly Interacting s- and p-Wave Fermi Gases*, Phys. Rev. Lett. **125**, 240402 (2020).

[76] S. Ding and S. Zhang, *Fermi-Liquid Description of a Single-Component Fermi Gas with p-Wave Interactions*, Phys. Rev. Lett. **123**, 070404 (2019).

[77] E. Haller, M. J. Mark, R. Hart, J. G. Danzl, L. Reichsöllner, V. Melezhik, P. Schmelcher, and H.-C. Nägerl, *Confinement-Induced Resonances in Low-Dimensional Quantum Systems*, Phys. Rev. Lett. **104**, 153203 (2010).

[78] S. Sala, P.-I. Schneider, and A. Saenz, *Inelastic Confinement-Induced Resonances in Low-Dimensional Quantum Systems*, Phys. Rev. Lett. **109**, 073201 (2012).

[79] S. Sala, G. Zürn, T. Lompe, A. N. Wenz, S. Murmann, F. Serwane, S. Jochim, and A. Saenz, *Coherent Molecule Formation in Anharmonic Potentials Near Confinement-Induced Resonances*, Phys. Rev. Lett. **110**, 203202 (2013).

[80] In q1D s-wave systems, the anharmonicity of the transverse confinement potential was observed [77,79] to induce couplings between the center-of-mass motion and the relative motion. This created new scattering resonances to bound states with c.m. excitation in the strongly confined direction [78]. However, we did not find any evidence of this effect in our data.

[81] Y. Nishida and S. Tan, *Confinement-Induced p-Wave Resonances from s-Wave Interactions*, Phys. Rev. A **82,** 062713 (2010).

[82] A complementary phenomenon can occur for scattering in mixed dimensions [81]. In that case, the odd parity of the c.m. motion can induce *p*-wave scattering in the relative coordinate, even though the underlying scattering is *s*-wave, because two atoms see different trapping potentials. In our case, the c.m. motion is irrelevant; instead, the odd parity of the relative motion in the strongly confined direction allows for the emergence of the even-wave scattering of identical fermions along the q1D direction.

[83] D. T. Son and E. G. Thompson, *Short-Distance and Short-Time Structure of a Unitary Fermi Gas*, Phys. Rev. A **81,** 063634 (2010).

[84] C. Ticknor, C. A. Regal, D. S. Jin, and J. L. Bohn, *Multiplet Structure of Feshbach Resonances in Nonzero Partial Waves*, Phys. Rev. A **69,** 042712 (2004).

[85] The cylindrically symmetric states are superpositions of Cartesian states with $n_x + n_z = 2\mathcal{N} + |m|$.

[86] The subleading correction modifies Δ_e by $1 - 2R_{3D}a_\perp^{-1} \times [\zeta(1/2) + \zeta(3/2)]$, such that the leading order gives roughly a 10% underestimate for our typical parameters.

[87] The subleading correction modifies Δ_o by $1 - 3R_{3D}\zeta(1/2)/a_\perp$, such that the leading order gives roughly a 20% underestimate for our typical parameters.

[88] This can be seen from Eqs. (9) and (11) since the 3D scattering volume scales as $V_{3D} \sim 1/B$ near the *p*-wave Feshbach resonance. The widening field range of correlations at higher lattice depths can be seen in Fig. 2, with the effect strongest for even-wave correlations in Fig. 2(b). There, even-wave correlations extend across a 3-G range at $V_L = 120\,E_R$, compared to a range of approximately 0.5 G of odd-wave correlations at similar lattice depth. Both of these are larger than the 0.2-G range of significant correlations observed in 3D.

[89] W. Zwerger, *The BCS-BEC Crossover and the Unitary Fermi Gas* (Springer, Berlin, 2012).

[90] I. Bloch, J. Dalibard, and W. Zwerger, *Many-Body Physics with Ultracold Gases*, Rev. Mod. Phys. **80,** 885 (2008).

[91] The numerical factors in $\tilde{C}$ are chosen such that the asymptotic momentum density $n_k \to \tilde{C}_o k_F/k^2$, when $\int (dk/2\pi)n_k = N$.

[92] Note that inhomogeneous transverse confinement broadens the range of a_o^{-1} for a given magnetic field, which makes the assignment of small $-1/k_F a_o$ ambiguous.

[93] S. A. Bender, K. D. Erker, and B. E. Granger, *Exponentially Decaying Correlations in a Gas of Strongly Interacting Spin-Polarized 1D Fermions with Zero-Range Interactions*, Phys. Rev. Lett. **95,** 230404 (2005).

[94] The subleading term of the isotropic Eq. (18) provides only a 50-mG correction to the leading order. Still, we determine B_0^y through a generalized form of Eq. (18) that includes anisotropic confinement [25].

[95] P. Makotyn, C. E. Klauss, D. L. Goldberger, E. A. Cornell, and D. S. Jin, *Universal Dynamics of a Degenerate Unitary Bose Gas*, Nat. Phys. **10,** 116 (2014).

[96] X. Yin and L. Radzihovsky, *Postquench Dynamics and Prethermalization in a Resonant Bose Gas*, Phys. Rev. A **93,** 033653 (2016).

[97] C. Eigen, J. A. P. Glidden, R. Lopes, E. A. Cornell, R. P. Smith, and Z. Hadzibabic, *Universal Prethermal Dynamics of Bose Gases Quenched to Unitarity*, Nature (London) **563,** 221 (2018).

[98] Due to anharmonicity of the optical lattice potential, there is some ambiguity in the experimental value of the transverse trap frequency. Since the lowest allowed excitation for even waves is the excitation of an atom from the first to third single-particle level of the optical lattice, the best choice for $\hbar\omega_\perp$ in this case is half that energy.

[99] T. Jeltes, J. M. McNamara, W. Hogervorst, W. Vassen, V. Krachmalnicoff, M. Schellekens, A. Perrin, H. Chang, D. Boiron, A. Aspect, and C. Westbrook, *Comparison of the Hanbury Brown–Twiss Effect for Bosons and Fermions*, Nature (London) **445,** 402 (2007).

[100] K. F. Thomas, Z. Ou, B. M. Henson, A. A. Baiju, S. S. Hodgman, and A. G. Truscott, *Production of a Highly Degenerate Fermi Gas of Metastable Helium-3 Atoms*, Phys. Rev. A **107,** 033313 (2023).

[101] L. Chomaz, I. Ferrier-Barbut, F. Ferlaino, B. Laburthe-Tolra, B. L. Lev, and T. Pfau, *Dipolar Physics: A Review of Experiments with Magnetic Quantum Gases*, Rep. Prog. Phys. **86,** 026401 (2023).

[102] Y. Cui, C. Shen, M. Deng, S. Dong, C. Chen, R. Lü, B. Gao, M. K. Tey, and L. You, *Observation of Broad d-Wave Feshbach Resonances with a Triplet Structure*, Phys. Rev. Lett. **119,** 203402 (2017).

[103] X.-C. Yao, R. Qi, X.-P. Liu, X.-Q. Wang, Y.-X. Wang, Y.-P. Wu, H.-Z. Chen, P. Zhang, H. Zhai, Y.-A. Chen, and J.-W. Pan, *Strongly Interacting Bose Gases Near a d-Wave Shape Resonance*, Nat. Phys. **15,** 570 (2019).

[104] L. Fouché, A. Boissé, G. Berthet, S. Lepoutre, A. Simoni, and T. Bourdel, *Quantitative Analysis of Losses Close to a d-Wave Open-Channel Feshbach Resonance in ^{39}K*, Phys. Rev. A **99,** 022701 (2019).

[105] L. Pricoupenko, *Modeling Interactions for Resonant p-Wave Scattering*, Phys. Rev. Lett. **96,** 050401 (2006).

[106] Z. Idziaszek, *Analytical Solutions for Two Atoms in a Harmonic Trap: p-Wave Interactions*, Phys. Rev. A **79,** 062701 (2009).

[107] V. Venu, P. Xu, M. Mamaev, F. Corapi, T. Bilitewski, J. P. D'Incao, C. J. Fujiwara, A. M. Rey, and J. H. Thywissen, *Unitary p-Wave Interactions between Fermions in an Optical Lattice*, Nature (London) **613,** 262 (2023).

[108] W. Schneider and M. Randeria, *Universal Short-Distance Structure of the Single-Particle Spectral Function of Dilute Fermi Gases*, Phys. Rev. A **81,** 021601(R) (2010).

[109] M. He and Q. Zhou, *p-Wave Contacts of Quantum Gases in Quasi-One-Dimensional and Quasi-Two-Dimensional Traps*, Phys. Rev. A **104,** 043303 (2021).

[110] C. Gao and Z. Yu, *Breathing Mode of Two-Dimensional Atomic Fermi Gases in Harmonic Traps*, Phys. Rev. A **86,** 043609 (2012).

[111] J. Hofmann, *Quantum Anomaly, Universal Relations, and Breathing Mode of a Two-Dimensional Fermi Gas*, Phys. Rev. Lett. **108,** 185303 (2012).

[112] Y.-C. Zhang and S. Zhang, *Strongly Interacting p-Wave Fermi Gas in Two Dimensions: Universal Relations and Breathing Mode*, Phys. Rev. A **95**, 023603 (2017).

[113] H. Hu and X.-J. Liu, *Resonantly Interacting p-Wave Fermi Superfluid in Two Dimensions: Tan's Contact and the Breathing Mode*, Phys. Rev. A **100**, 023611 (2019).

[114] A. M. Rey, G. Pupillo, C. W. Clark, and C. J. Williams, *Ultracold Atoms Confined in an Optical Lattice Plus Parabolic Potential: A Closed-Form Approach*, Phys. Rev. A **72**, 033616 (2005).

[115] P. B. Blakie, A. Bezett, and P. Buonsante, *Degenerate Fermi Gas in a Combined Harmonic-Lattice Potential*, Phys. Rev. A **75**, 063609 (2007).